Ocean Modelling 145 (2020) 101532

Contents lists available at ScienceDirect

Ocean Modelling

journal homepage: www.elsevier.com/locate/ocemod

Applications of an unstructured grid surface wave model (FVCOM-SWAVE) to the Arctic Ocean: The interaction between ocean waves and sea ice

Yang Zhang [a,b,*], Changsheng Chen [c], Robert C. Beardsley [d], William Perrie [e], Guoping Gao [a,f], Yu Zhang [a], Jianhua Qi [c], Huichan Lin [c]

[a] College of Marine Sciences, Shanghai Ocean University, Shanghai, China
[b] State Key Laboratory of Satellite Ocean Environment Dynamics, Second Institute of Oceanography, MNR, Hangzhou, China
[c] School for Marine Science and Technology, University of Massachusetts-Dartmouth, New Bedford, MA 02744, USA
[d] Department of Physical Oceanography, Woods Hole Oceanographic Institution, Woods Hole, MA 02543, USA
[e] Fisheries & Oceans Canada, Bedford Institute of Oceanography, Dartmouth, Nova Scotia, Canada
[f] College of Ocean Science and Engineering, Shanghai Maritime University, Shanghai, China

ARTICLE INFO

Keywords:
Arctic Ocean
Wave attenuation
Ice breakage
Ocean modeling
Positive feedback

ABSTRACT

Rapidly melting sea ice processes during the summer tend to enlarge the open water in the Arctic region. The resulting larger potential fetch for surface waves can allow significant wave generation and development in the region. The sea ice plays an energy dissipation role for waves propagating into the ice-covered sea. A spherical-coordinate surface wave model was established within the unstructured grid Finite-Volume Community Ocean Model (FVCOM) to examine the influence of ice-induced wave attenuation on waves propagating into the ice in the Arctic Ocean. Ice-induced wave attenuation parameterizations were implemented, with an effective methodology to reduce numerical dissipation during the energy advection in geographic space. Wave partition and source tracking methods were added to distinguish the windsea and swell, as well as to backtrack swell waves to their sources. The model-simulated significant wave heights and peak periods were compared with available buoy and Jason-2 satellite measurements. Results from a process-oriented model show that simulations of the surface waves in the Arctic region are improved when ice-induced attenuation is included in the model system. An empirical method is used to statistically estimate wave-induced ice breakage, based on the wave-induced internal ice strain, as waves penetrate into the ice zone. The simulation results support the 'ice retreat-wave growth' positive feedback mechanism.

1. Introduction

The Arctic Ocean (Fig. 1) has been in a rapidly-changing phase since the latter half of the 20th century (Stephenson et al., 2011; Comiso, 2006; Comiso et al., 2008). The sea ice extent in the summer through fall has decreased at an average rate of about 3.8×10^5 km^2 per decade since 1978 (Cavalieri et al., 2003; Meier et al., 2005). The minimum ice extent in September was 7.2×10^6 km^2 in 1979 and dropped to 4.7×10^6 km^2 in 2018, with an extremely low coverage of 4.3×10^6 km^2 in 2007 and an even lower coverage of 3.6×10^6 km^2 in 2012. This trend toward a larger summer open water area in the Arctic Ocean has produced potentially enlarged fetches for the growth of wind-induced surface waves. As a result, wave–ice interactions have become a dynamically important process, not only for the breaking of ice floes and the melting of ice, but also for wave generation, propagation and dispersion in the Arctic basin and coastal regions (Squire et al., 2009; Williams et al., 2013b).

To our knowledge, there have been few studies done on wave–ice interactions in the Arctic Ocean. Kohout et al. (2014) compared the change of the significant wave heights with the variation of the ice-edge latitude in the Antarctic Sea and found that the ice retreat correlated well with the development of the waves. Compared with the Southern Ocean, the Arctic Ocean is quite different because the maximum fetch for wave growth is limited. Although maximum fetches for wave growth in the Norwegian Sea, Barents Sea and Greenland Sea have remained essentially unchanged, the fetches have become larger in the Pacific Pan-Arctic region (Collins et al., 2015). Moreover, winds have also changed slightly. During the period of 1971–2013, from June through September, the winds have intensified by only 0.1–0.3% per year, whereas the average significant wave height grew by 3.0–4.1%

* Correspondence to: State Key Laboratory of Satellite Ocean Environment Dynamics, Second Institute of Oceanography, MNR, 36 North Baochu Road, Hangzhou, China.
E-mail addresses: yzhang@sio.org.cn (Y. Zhang), c1chen@umassd.edu (C. Chen), rbeardsley@whoi.edu (R.C. Beardsley), william.perrie@dfo-mpo.gc.ca (W. Perrie), gpgao@shmtu.edu.cn (G. Gao), yuzhang@shou.edu.cn (Y. Zhang), jqi@umassd.edu (J. Qi), hlin@umassd.edu (H. Lin).

https://doi.org/10.1016/j.ocemod.2019.101532
Received 25 July 2018; Received in revised form 29 August 2019; Accepted 14 November 2019
Available online 20 November 2019

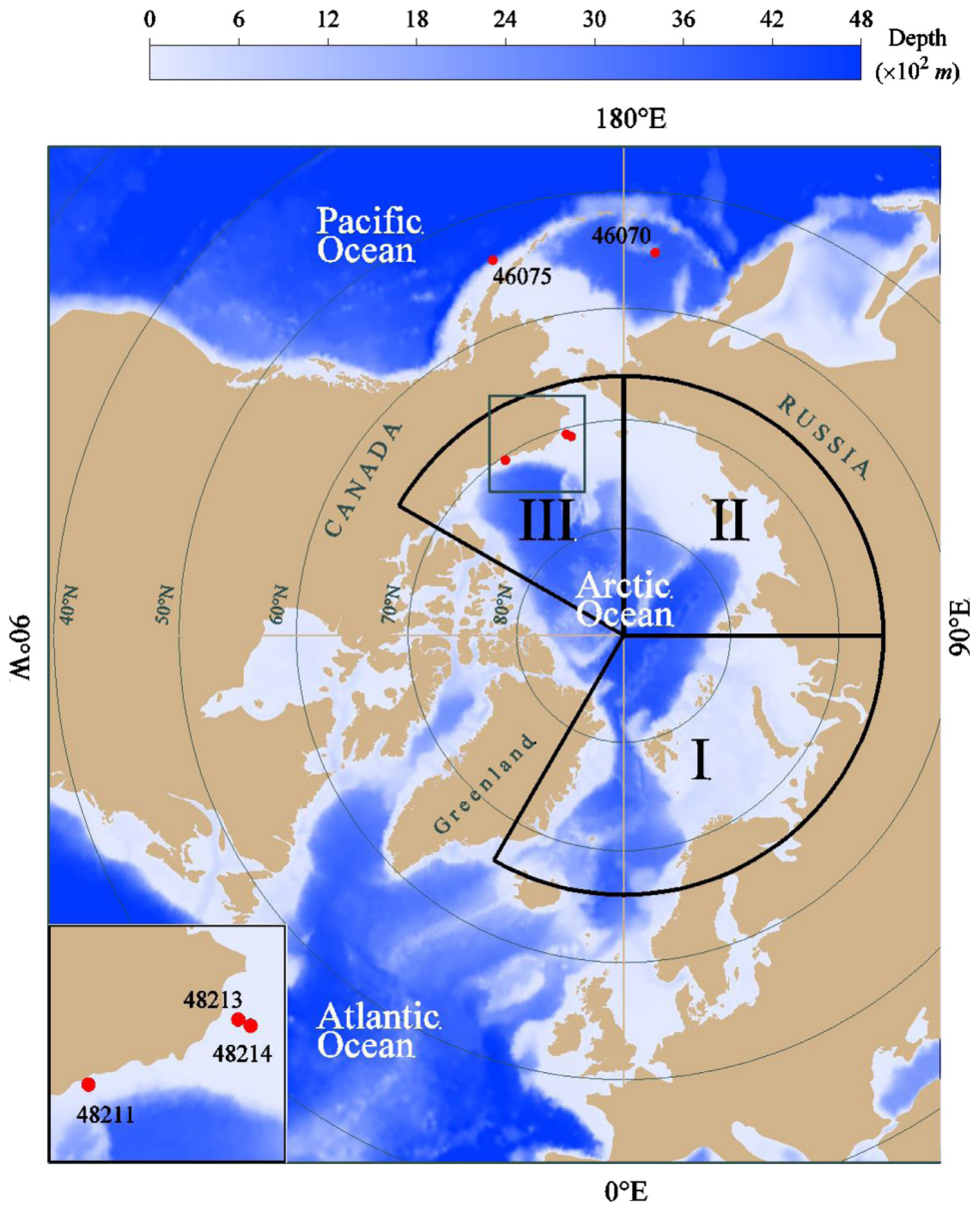

Fig. 1. Geometry of the Arctic Ocean and the adjacent Pacific and Atlantic Oceans. Red dot: The locations of buoy stations where the wave records are used in this study. Digital number beside individual red dot is the station ID. The zoomed-in map in the black square of the north of Alaska is shown in the bottom left corner. Labels I, II and III indicate the three sectors covering the regions of 30°W–90°E, 90°E–180°E, and 120°W–180°W, respectively.

per year, and the averaged peak period increased by 0.5–0.8% per year (Wang et al., 2015). As a result of the ice retreat, the enlarged maximum potential fetch favors increased wave growth in the Pacific Pan-Arctic region and thus increased wave generation and propagation in the Arctic Ocean. The recent Sea State Boundary Layer Experiment by Thomson et al. (2016) (http://www.apl.washington.edu/project/project.php?id=arctic_sea_state) produced a new dataset for wave–ice interaction studies. This dataset provides the basis for a new set of model studies.

The Arctic has limited monitoring sites for surface waves. Due to severe natural conditions and difficulties in deploying and maintaining instruments to measure waves in the MIZ, numerical wave models have become a popular tool to examine the ice–wave interactions in the Arctic Ocean. There are only a few such wave models that cover the partial or entire Arctic Ocean. One example is the global NOAA WAVEWATCH III (NWWIII), which has a computational domain bounded by 77°S–77°N and is configured on a structured spherical rectangular grid with a $1.25° \times 1.00°$ horizontal resolution (Tolman et al., 2002; Tolman and the WAVEWATCHIII®Development Group, 2014). This model has been placed into 24/7 forecast operations as an ensemble system driven by the operational Global Data Assimilation Scheme (GDAS) and the aviation cycle of the Medium Range Forecast model (http://polar.ncep.noaa.gov/waves/implementations.shtml) (Tolman and the WAVEWATCHIII®Development Group, 2014; Thomson and Rogers, 2014). A second example is the 1979–2009 NOAA CFSR wave hindcast product (WAVEWATCH III® 30-year Hindcast Phase 2). It has included global and Arctic Ocean curvilinear grids with the horizontal resolutions of 30 and 15 mins, respectively (https://polar.ncep.noaa.gov/waves/hindcasts/nopp-phase2.php). Thirdly, the European Center for Medium Range Weather Forecasting wave model (named ECWAM) was configured to cover the entire Arctic Ocean with the inclusion of the North Pole (Bidlot, 2012; ECMWF, 2014).

Li and Saulter (2014) made a multi-resolution implementation of WWIII for the entire Arctic Ocean using a spherical multiple-cell (SMC) grid. This model was designed to relax the CFL restriction of the Eulerian advection time step at high latitudes by merging the conventional latitude-longitude grid cells. Their approach was also designed to overcome the North Pole singularity issue. Similar works were also

done recently; Casas-Prat et al. (2018) conducted a CMIP5-based global wave climate projections. In addition to the global-scale WWIII model, there are several regional wave models established for the Arctic Ocean or adjacent coastal areas. One example is the WWIII-based Alaskan Waters Model with a computational domain covering a portion of the Bering Sea, Alaska coast and the Beaufort Sea (Chao et al., 2004).

Various theories and observation-based methods, such as the scattering, viscous and mass-loading models, have been proposed to simulate wave evolution and dissipation in the ice-covered sea (Peters, 1950; Keller and Weitz, 1953; Shapiro and Simpson, 1953; Wadhams et al., 1986; Weber, 1987; Liu and Mollo-Christensen, 1988; Liu et al., 1991; Squire et al., 1995; Perrie and Hu, 1996; Meylan and Masson, 2006; Dumont et al., 2011a,b; Doble and Bidlot, 2013; Williams et al., 2013a,b; Li et al., 2015). The basic difference among these methods is the manner in which the ice field is defined. One approach follows a scattering method formulation, in which the ice field is treated as individual ice floes with the inclusion of wave energy attenuation, reflection and transmission. An alternate approach, which is valid for different sea ice situations, is to consider the ice as a continuous material covering the sea surface, and wave attenuation is parameterized in terms of empirical formulations, assuming parameterizations for ice viscosity, ice strain, and deformation rates. For mass-loading models, the ice field is treated as composed of mass points, which exert pressure on the sea surface but no coherence or rheological properties are assumed (Squire et al., 1995; Squire, 2007).

In the recent years, the wave–ice interaction process and ice-induced attenuation have been implemented into WWIII (Tolman, 2003, 2009; Tolman and the WAVEWATCHIII®Development Group, 2014). There are three options for wave damping by the sea ice. The first option is the damping of wave energy by a pre-determined uniform attenuation coefficient in the frequency space. The other two options assume the ice is a thin elastic plate or a viscous-elastic layer, and the wave energy is attenuated non-uniformly in the frequency space (Tolman and the WAVEWATCHIII®Development Group, 2014). A model simulation of the storm-generated large waves in the Arctic Ocean has revealed that further reductions in seasonal ice cover tend to result in larger waves, which in turn provides a mechanism to break up sea ice and accelerate ice retreat (Thomson and Rogers, 2014). Following Kohout and Meylan (2008), an attenuation scheme for wave–ice interactions, particularly in the range of periods of 6–16 s, was implemented into the ECWAM. This model was applied to simulate the waves in the sea ice off Antarctica (Doble and Bidlot, 2013). The upper-bound of the wave period was selected on the basis of wave observations in the Antarctic marginal ice zone (MIZ), which showed that waves with periods of >16 s experienced very low attenuation (Kohout et al., 2014). This finding, however, was only applied to the marginal ice zone, in which the ice concentration was relatively low. Squire et al. (2009) proposed an ice-induced wave attenuation coefficient formulation for waves with periods longer than 10 s This formulation can resolve the penetration of longer period waves into the ice-covered Arctic waters across the MIZ. In fact, ice-induced wave decay has previously been suggested to be a function of sea ice properties, such as ice thickness, ice concentration, and the size of ice floes (Perrie and Hu, 1996; Meylan and Masson, 2006).

The unstructured grid Finite-Volume Community Ocean Model (FVCOM) is an unstructured-grid, finite-volume coupled ice–ocean–wave model originally developed by Chen et al. (2003) and improved by the FVCOM team and users (Chen et al., 2006, 2013). This model has been configured for the Arctic and global Oceans to establish the Arctic/Global Ocean Finite-Volume Community Ocean Model (AO-FVCOM/Global-FVCOM) (Chen et al., 2009; Gao et al., 2011; Chen et al., 2016). The AO-FVCOM/Global-FVCOM contains an unstructured-grid sea ice model (UG-CICE, (Gao et al., 2011)) and surface wave model (SWAVE Qi et al., 2009), which were developed on the framework of the structured-grid versions of CICE (Hunke and Lipscomb, 2006) and the Simulation Waves Nearshore (SWAN) model (Booij et al., 1999; SWAN Team, 2006a,b), respectively. The ice and ocean were fully coupled within FVCOM but the ice–wave interactions have not been formulated until this study.

Our effort is to configure SWAVE for global and basin-scale Arctic Ocean applications, with an inclusion of the North Pole in the spherical coordinate system. Moreover, our studies focus on the influences of ice-induced wave attenuation on the generation, propagation and dissipation of surface waves in the Arctic Ocean. An effective methodology is introduced to reduce numerical dissipation during the energy advection in geographic space. A series of numerical experiments are made to validate SWAVE through comparisons with observed significant wave heights and periods. The wave-induced ice breakage and an 'ice retreat-wave growth' positive feedback mechanism is examined, based on the validated results.

The remaining text is organized as follows. In Section 2, the Global-Arctic Ocean-SWAVE model is described, with a focus on the implementation of ice-induced wave attenuation. In Section 3, model-data comparisons at available buoy sites and satellite strips are presented. A discussion is given in Section 4, and conclusions are summarized in Section 5.

2. The Arctic Ocean SWAVE and design of numerical experiments

The Arctic Ocean SWAVE was developed under the framework of FVCOM by Qi et al. (2009). The finite-volume advection scheme used in SWAVE performs with the same numerical accuracy as the third-order finite-difference method used in SWAN (Qi et al., 2009). To apply SWAVE for the Arctic/global Ocean, we made the following modifications. First, a coordinate projection method is improved to solve the singularity issue at the North Pole and the meridian convergence problem at high latitude. Second, an ice-induced wave attenuation parameterization is designed and added to the form of the action density flux term over geographic space in the wave spectral action balance equation. The treatment and method used in the first part are derived and discussed in Appendix A; the formulation for the second part and design of numerical experiments are described below.

2.1. Ice-induced wave attenuations

In spherical coordinates, the wave growth and dissipation are governed by the wave action density spectrum balance equation given as

$$\frac{\partial N}{\partial \gamma}+\frac{1}{R\cos\lambda}\left\{\frac{\partial\left[\left(C_{g,\lambda}+u\right)N\right]}{\partial\lambda}+\frac{\partial\cos\varphi\left[\left(C_{g,\varphi}+v\right)N\right]}{\partial\varphi}\right\}+\frac{\partial C_\sigma N}{\partial\sigma}+\frac{\partial C_\theta N}{\partial\theta}=\frac{S_{tot}}{\sigma}, \tag{1}$$

where N is the wave action density spectrum; σ is the relative frequency; θ is the wave direction; C_σ and C_θ are the wave propagation velocities in spectral space (σ, θ); γ, λ and φ are the time, longitude (zonal) and latitude (meridian), respectively; $C_{g,\lambda}$ and $C_{g,\varphi}$ are the zonal and meridian components of the wave group velocity; u and v are the zonal and meridian components of the ambient ocean current velocity. S_{tot} is the source–sink term given as

$$S_{tot}=S_{in}+S_{nl3}+S_{nl4}+S_{ds,w}+S_{ds,b}+S_{ds,br}+S_{att,ice}, \tag{2}$$

where S_{in} is a function for the wind-induced wave growth; S_{nl3} is the nonlinear transfer of wave energy due to triadic three-wave interactions; S_{nl4} is the nonlinear transfer of wave energy due to four-wave interactions; $S_{ds,w}$, $S_{ds,b}$, and $S_{ds,br}$ are the three wave energy dissipation terms which represent the wave energy dissipation due to white capping, bottom friction, and depth-induced wave breaking, respectively; and $S_{att,ice}$ is the ice-induced wave attenuation term.

The empirical formula of $S_{att,ice}$, which has been used in previous studies (Doble and Bidlot, 2013; Williams et al., 2013a,b), is a dissipation function as given as

$$N\left(\theta,\sigma,t_{n+1}\right)=N\left(\theta,\sigma,t_n\right)\exp\left(-\beta C_g\Delta t\right), \tag{3}$$

where β is the dimensional attenuation coefficient; $\Delta t = t_{n+1} - t_n$ and subscript "n" presents the nth time step; and C_g is group velocity. Following the approach used in previous modeling works (Dumont et al., 2011a,b; Williams et al., 2013a,b; Ardhuin et al., 2016), we use the ice-free dispersion relation $\omega^2 = gk\tanh(kd)$ in our present model. Here, ω is the wave angular frequency, g is the gravitational acceleration, k is the wave number and d is the water depth. The transport speed C_g of wave energy is assumed to be the same in the ice-covered sea as in the open ocean (Dumont et al., 2011a,b; Williams et al., 2013a,b; Ardhuin et al., 2016). The exponential decay function in Eq. (3) was developed based on the observational evidence from various types of measurements (Robin, 1963; Dean, 1966; Wadhams et al., 1988; Squire and Moore, 1980; Liu et al., 1991), with a summary given by Kohout and Meylan (2008) (hereafter referred to as KM08). These measurements show that wave energy decays exponentially with distance as it travels into the marginal ice zone.

On each finite control volume (CV) in the ice-covered sea, based on Eq. (3), the total wave energy should be damped by a factor of $\exp(-\beta C_g \Delta t)$. This approach works for the case in which the wave energy is uniformly distributed. In the MIZ where the wave energy gradient is large, however, it might lead to an unrealistic result if the traveling distance of wave energy is calculated by discrete-determined group velocities. Let us assume that N′ is the wave energy newly added into an ice-covered CV over a time interval Δt. According to Eq. (3), in the main loop of the model, N′ will be attenuated after the advection. In the discrete finite volume method, the traveling distance (Δr) of N′ is actually the distance between the centroids of the adjacent CVs, which might differ from the true distance traveled at the wave group velocity ($C_g \Delta t$). If $C_g \Delta t \ll \Delta r$, the width of the wave attenuation zone calculated by Eq. (3) can be underestimated, and vice versa. This is a typical numerical dissipation issue that needs to be taken into account when Eq. (3) is used. It is more reasonable to calculate the attenuation rate by considering the distance that the wave energy really travels over one time step. To do this, we re-designed $S_{att,ice}$ with Eq. (4) given as

$$N(\theta,\sigma,t_{n+1}) = N(\theta,\sigma,t_n) - \frac{\Delta R}{\Omega}\sum_{i=1}^{l} N'_i\left(1-\exp\left(-\beta\Delta r_i\right)\right)\Delta l_i, \tag{4}$$

where N'_i is the newly added wave energy to the CV; l is the number of the groups of newly added wave energy to the CV; ΔR are the distances from a triangle's node to the triangle centroids connected to this node; Ω is the area of the CV with its center at an individual triangle node and bounded by the sections linked to the centroids and the mid-point of the adjacent sides in the surrounding triangles; Δl_i are the perimeters of Ω; Δr_i are the traveling distances of newly added wave energy, which are defined as the distances between the centroids of the adjacent control volumes.

In Eq. (4), β is a function of wave period and direction, as well as ice concentration and floe size. In general, it can be expressed as

$$\beta = C_i \frac{\alpha}{\overline{D}}, \tag{5}$$

where α is a non-dimensional attenuation coefficient; C_i is the average ice concentration of the two adjacent control volumes; and $\overline{D}$ is the average diameter of the floes (Doble and Bidlot, 2013). In SWAVE, C_i can be determined either from observations or ice models, and $\overline{D}$ can be specified on the basis of the so-called fragility parameter (probability of ice breakage) and the specification of the minimum and maximum floe sizes, as described by Dumont et al. (2011a,b) and Doble and Bidlot (2013). In this study, following Doble and Bidlot (2013), the number of the fragmentation steps M is given as

$$M = \left[log_{\varepsilon}\left(D_{max}/D_{min}\right)\right], \tag{6}$$

where ε determines the number of pieces that each floe will be fragmented into, and is set to be 2. D_{max} and D_{min} are the maximum and minimum floe diameters, respectively. The mean floe diameter is calculated by

$$\overline{D} = \frac{\sum_{m=0}^{M}\left(\varepsilon^2 f\right)^m \varepsilon^{-m} D_{max}}{\sum_{m=0}^{M}\left(\varepsilon^2 f\right)^m}, \tag{7}$$

where f is the possibility of the ice floe fragment and is set to be 0.9. $\overline{D} \approx 36$ for D_{max} and D_{min} are given as 200 and 20, respectively, and $M \approx 3$.

α describes the attenuation rate per ice floe that the wave encounters. Observations have suggested that this coefficient is a function of wave period (T) and ice floe thickness (h). KM08 derived an elastic plate model and used it to predict a logarithm distribution for α versus T in the wave period range of 6–16 s and ice floe thickness h in a range of 0.4–3.2 m (see Fig. 8 in KM08, re-drawn in Fig. 2 in this paper). Compared with those obtained from the theoretical formulations derived by Wadhams et al. (1988) and Masson and LeBlond (1989), the parameterization of α derived by KM08 has provided credible results for capturing observed wave attenuation in the Greenland Sea. This method was used by Perrie and Hu (1996) for case studies in the Labrador Sea. Implementing KM08-derived ice-induced wave attenuation into WAM, Doble and Bidlot (2013) found that this model was capable of reproducing the wave measurements of buoys in the MIZ and nearby ice-covered areas off Antarctica. They also reported that adding an additional sea ice 'drag attenuation' could weaken the wave energy into the MIZ, and thus improve the simulated waves over certain time periods. The dissipation term is $\alpha_{v\_d} = C_d H k^2$, in which C_d is the constant ice–wave drag coefficient given as 1×10^{-2} and H is the wave height of a given wave component. Ardhuin et al. (2016) deployed a dissipation term based on the under-ice laminar friction theory (Liu and Mollo-Christensen, 1988). The dissipation rate is $\alpha_{v\_a} \cong k\sqrt{v\omega}/C_g$, in which k is the wave number; $v \cong 1.83\times10^{-6}$ m^2/s, and represents the molecular viscosity at the freezing temperature of sea water; ω is the angular frequency; and C_g is the group velocity. An experiment for idealized cases is established to evaluate the contributions of α_{v_d} and α_{v_a} to the significant wave height in the ice-covered sea. The simulation results indicate that α_{v_a} is negligible, while α_{v_d} significantly decreases the significant wave heights (not shown here). We have adopted the KM08-derived parameterization for the non-dimensional wave attenuation coefficient α in SWAVE for the wave period range of 6–16 s (Fig. 2), with the understanding that other attenuation mechanisms can be added in the future, with careful validations.

The ice floe thickness (h) in KM08, required to determine α, can be estimated from an ice model or from satellite measurements. Krinner et al. (2010) also proposed an empirical formulation in the form of

$$h = a_0 + \left(a_1 + a_2\, C_i\big|_{min}\right)\left(a_3 + a_4\left(C_i - C_i\big|_{min}\right)\right), \tag{8}$$

where $C_i\big|_{min}$ is the minimum value of C_i. In real cases, we assume that $C_i\big|_{min} = 0$ if $C_i < 1.0$ and $C_i\big|_{min} = 1.0$ if $C_i = 1.0$. $(a_0, a_1, a_2, a_3, a_4)$ are the constants given as (0.0, 0.2, 2.8, 1.0, 2.0), respectively. Recently, Zhang et al. (2016b) collected the ice thickness data available in the Arctic Ocean for the model validation, from ICESat (the ice, cloud, and land elevation satellite campaigns over the period 2003–2008) (Kwok et al., 2009); EM-Airbone (the electromagnetic airborne measurements) over the period 2001–2009 (Haas et al., 2009); Romanov-Atlas (the atlas of ice and snow of the Arctic basin and Siberian shelf seas over period 1978–1989 Romanov, 1995); and Coastal-Stations (the drill-hole, fast sea ice thickness measurements at 51 coastal stations over the period 1998–2008) (A. Proshutinsky, personal communication). Most of these measurements include relatively large uncertainties that are not quantitatively estimated and do not cover our 2013 simulation period. We collected the Cryosat −2 monthly averaged remote-sensing data over October 2013 and compared satellite-derived sea ice thickness with Eq. (8)-derived h values with respect to ice concentration. The results show that Eq. (8)-derived h remain around the lower-bound of the observed sea ice thickness in the range of $C_i < 1.0$. However, this value overestimates sea ice thickness at $C_i = 1.0$ (Fig. 3a). We also

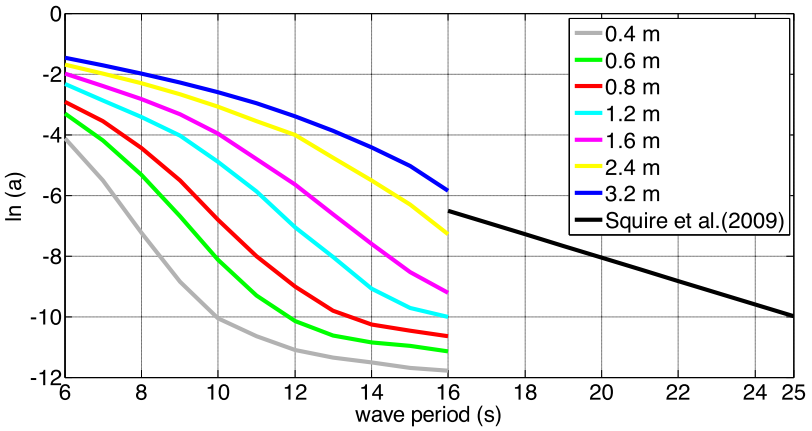

Fig. 2. The re-plotting of the logarithm of the non-dimensional attenuation coefficients [ln(α)] versus wave period [T (sec)] in a range of 6–16 s proposed by KM08 and in a range of 16–25 s proposed by Squire et al. (2009). The numbers listed in the upper-right corner are the ice thickness (h).

made the same comparison with the 'Coastal-Stations' measurements, and the results are similar (Fig. 3b). In spite of these incongruences, this empirical equation reasonably represents the trend of the sea ice thickness with respect to the sea ice concentration. To capture the mean value of the sea ice thickness variation via the sea ice concentration recorded on either satellites or coastal stations, we modified Eq. (8) by adjusting (a_0, a_1, a_2, a_3, a_4) to be (0.4, 0.2, 1.4, 1.0, 2.0), respectively (Fig. 3).

The KM08-formulation for α was designed for wave periods in the range of 6–16 s. For real ocean applications, such as when the wave period is shorter than 6 s, we used an α value of 6 s. In the Arctic, the waves with a period of >16 s can penetrate deeply within the MIZ and the pack-ice area (Squire et al., 2009), which may influence both the ice properties and wave fields across the MIZ and in the ice-covered region. To take this effect into account, we have adopted the empirical wave attenuation formulation suggested by Squire et al. (2009) for the case when wave periods exceeded 16 s (see Fig. 2). This formulation is given as

$$\beta = 0.02 * \exp(-0.386T). \quad (9)$$

Thus, the dimensional attenuation coefficient β is derived from the combination of the two wave attenuation schemes according to the wave periods. Generally, the higher frequency wave energy decays faster, while in the directional domain, the wave energy is uniformly attenuated. It should be noted that both attenuation mechanisms are old; but they are well validated and therefore appropriate for numerical simulations. New parameterization schemes can be implemented in the future with careful validations.

2.2. Design of numerical experiments

The Arctic Ocean SWAVE (hereafter referred to as AO-SWAVE) model was configured using the same Global-Arctic Ocean nested unstructured grid as that of AO-FVCOM (Fig. 4) (Chen et al., 2016; Zhang et al., 2016a). The horizontal resolution in the computational domain varies from ~2 km near the coast and around the islands to 40 km in open ocean areas. The AO-SWAVE can run either using the Arctic Ocean subdomain grid through nesting with the global-domain SWAVE or by merging the Arctic Ocean subdomain grid to the global domain as a single global-scale model. In our experiments, we ran AO-SWAVE as a single global-scale model and focused our analysis in the Arctic Ocean subdomain only. The ice concentration used in AO-SWAVE is the daily SSM/I and SSMIS data produced by Remote Sensing Systems and sponsored by the NASA Earth Science MEaSUREs Program, with a spatial resolution of 12.5 km (Wentz, 2013).

To quantify the contribution of the ice-induced wave attenuation, we made numerical experiments for cases with and without the ice-induced wave attenuation. In Case I, the ice concentration was taken

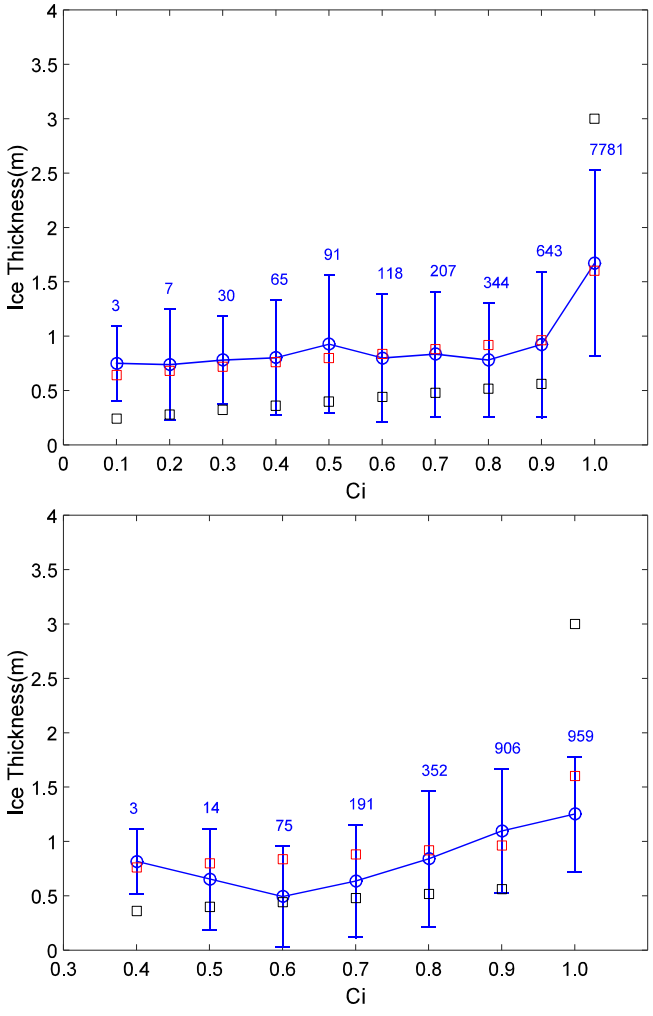

Fig. 3. Comparisons between the empirically calculated and observed sea ice thickness values (unit: m). Upper panel: the Cryosate-2 monthly averaged remote-sensing data; lower panel: the "Coastal Stations" data. Black open box: the results obtained using the original empirical function. Red open box: the results obtained using the modified empirical function with adjusted parameters.

into account in the wind forcing exerted at the sea surface through the following formulation:

$$\vec{\tau}_{\text{wind,input}} = \vec{\tau}_{\text{wind,real}}(1 - C_i), \quad (10)$$

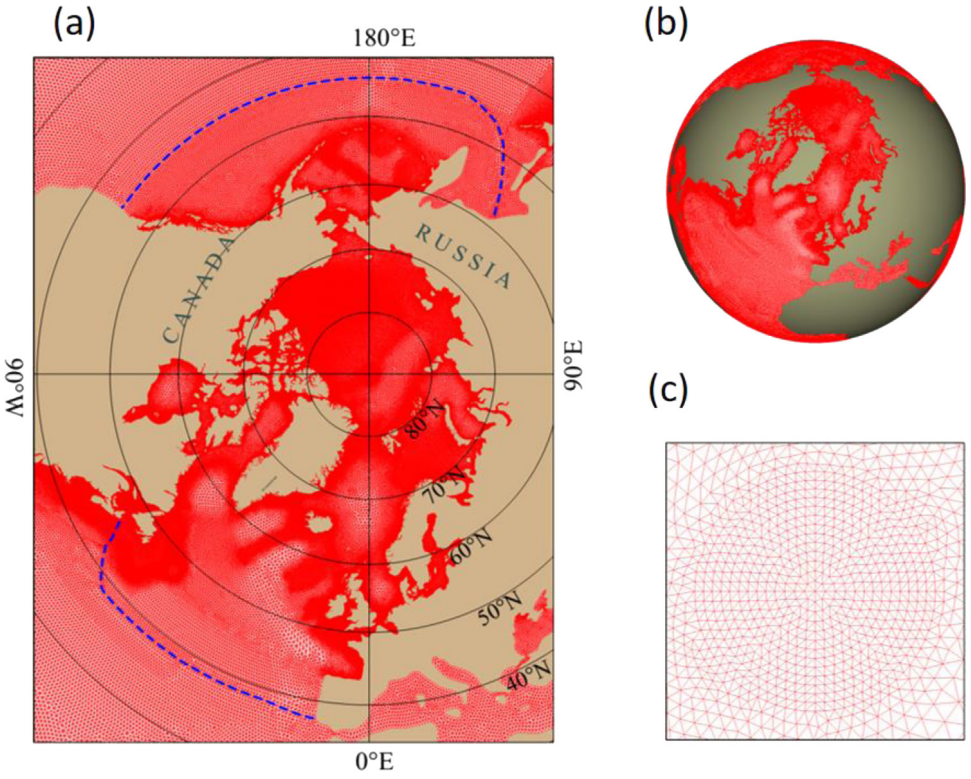

Fig. 4. The triangular grids used for the FVCOM-SWAVE model. (a) The Arctic Ocean subdomain grid that can be run either through nesting to the Global domain or as a part of the Global-SWAVE grid; (b) the Global-SWAVE grid; and (c) the grid around the North Pole.

Table 1
IDs, positions and data availability of observational stations.

Station ID	Longitude	Latitude	Location	Data Source
46070	175.27W	55.08N	Bering Sea	NCEI
46075	160.806W	53.926N	Offshore Aleutian islands	
48211	146.038W	70.37N	Beaufort Sea inshore	
48213	164.084W	70.522N	Chukchi Sea inshore	NDBC
48214	165.249W	70.872N	Chukchi Sea offshore	

where $\vec{\tau}_{wind,input}$ is the input wind stress at the ice–sea interface; $\vec{\tau}_{wind,real}$ is the wind stress calculated based on the National Center for Environmental Prediction and the National Center for Atmospheric Research (NCEP/NCAR) dataset (Zhang et al., 2016a). The other parameters for S_{in} remain the same as the default setup for SWAVE. In this case, the experiment was made with inclusion of the parameterization for ice-induced wave attenuation. In Case II, the ocean was treated as ice-free, and the experiment did not include the ice concentration in the wind forcing field or the ice-induced wave attenuation parameterization. In Case III, the ice concentration was taken into account for the wind input term in the action conservation Eqs. (1) and (2), but no ice-induced wave attenuation was considered. For all 3 cases, directions were divided into 36 equally distributed angular bins, and frequencies were distributed exponentially in 40 bins in the range of 0.04–1.0 Hz. We have adopted the wave-partitioning program from WWIII and implemented it in SWAVE. This program was used to separate windsea and swell waves in the wave simulation.

The model results were compared with observed wave data available at buoys in the Arctic Ocean and adjacent regions. The locations of the fixed buoys are listed in Table 1 and shown in Fig. 1. Our major interests are to examine how the sea ice influences the wave energy distribution in the Arctic Ocean and to evaluate the AO-SWAVE performance. For this purpose, we ran the simulations for the three cases for the period from 00:00:00 June 1 to 24:00:00 October 31, 2013, during which time wave measurements were available at buoys #48211, 48213 and 48214. All the buoy data were downloaded from the database of National Data Buoy Center (http://sdf.ndbc.noaa.gov/) and the National Centers for Environmental Information (https://www.ncei.noaa.gov/). Significant wave height (SWH) data from the Jason-2 program (ftp://avisoftp.cnes.fr/AVISO/pub/jason-2/) were also used for comparisons in the North Atlantic Ocean and North Pacific Ocean. The model was also run for the period from 00:00:00 June 1 to 24:00:00 October 31, 2014, during which time wave data were collected in the Beaufort Sea using three Surface Wave Instrument Floats with Tracking buoys (SWIFTs) (Smith and Thomson, 2016).

3. Model assessment

3.1. Model-data comparisons in the Bering Sea of the Pan-Arctic Ocean

The model-data comparisons were made for stations #46070 and #46075 in the Bering Sea, the Pacific Ocean of the pan-Arctic region and the Jason-2 satellite derived data in the high-latitude region between 55°N to 66°N. The purpose of these comparisons was to determine if the model can reliably simulate ocean surface waves on the Pan-Arctic scale, which is essential if swell waves in the Arctic Ocean were to be discussed. The comparisons were first made for significant wave heights (SWH) and peak periods (T_{peak}), and then for wind sea and swell waves.

For Case I, the model-data comparisons shown in Fig. 5 suggest that the model is capable of reproducing the SWH temporal variability observed at these two stations, with correlation coefficients of 0.75 and 0.91, biases of 0.10 m and 0.19 m, and root-mean-square error (RMSE) of 0.82 m and 0.56 m at #46070 and #46075, respectively (Table 2). The correlation was estimated with a significant testing at a P-value of <0.01. The linear regression function of the computed SWHs with respect to observed SWHs had a slope of 0.9, with an intercept of 0.13 m at #46070 and 0.03 m at #46075. SWAVE showed relatively *larger* errors in T_{peak} than in SWH, although the model did reasonably resolve the temporal variability of T_{peak}. The linear regression function of the

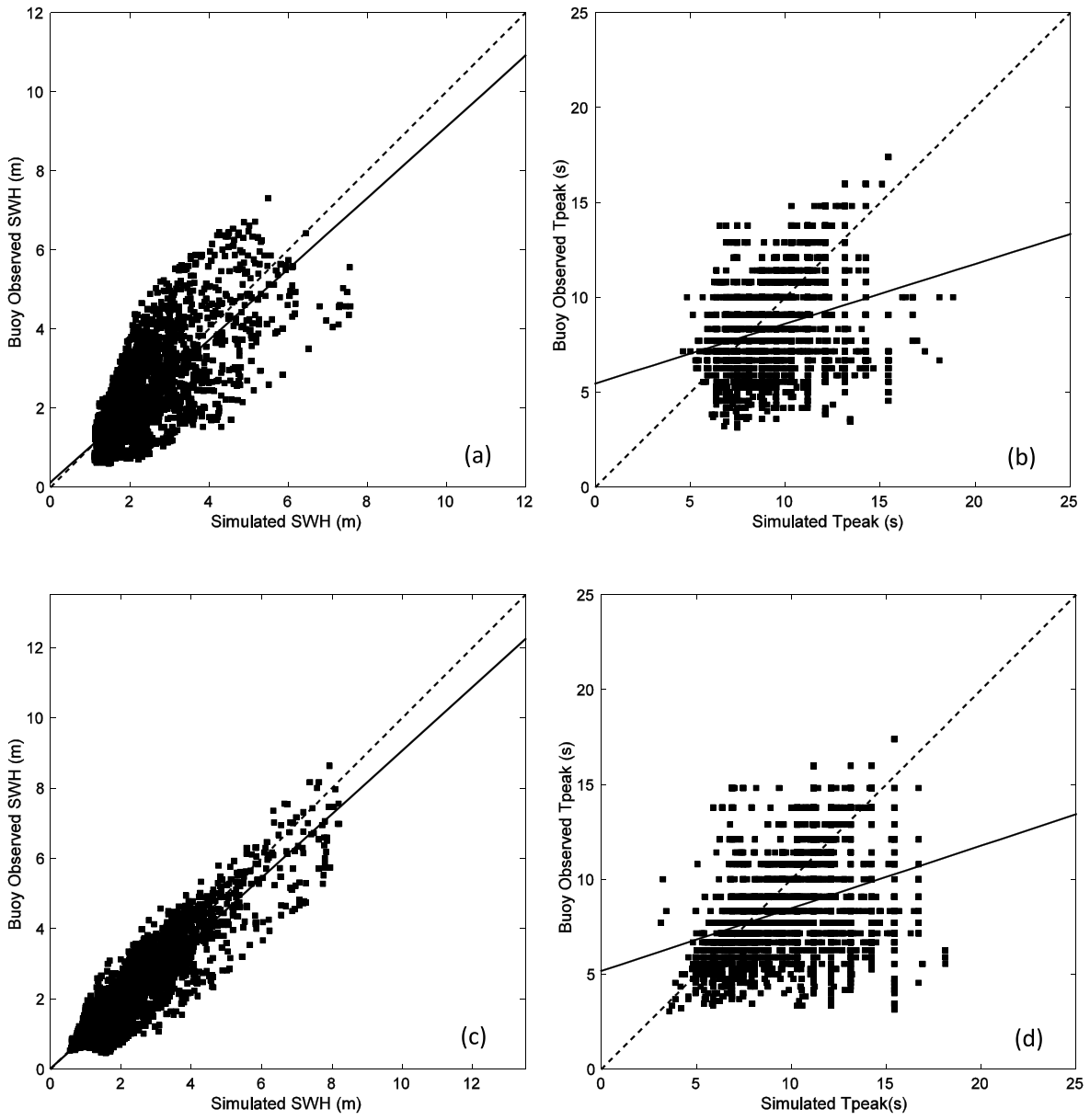

Fig. 5. Comparisons of model-computed and buoy-observed SWHs (Left two panels) and peak periods (Right two panels) at stations #46070 (Upper two panels) and #460705 (Lower two panels) over the time period June–October, 2013.

Table 2
Bias, correlation coefficient, slope, intercept, standard derivation (STD) and root mean square error (RMSE) of the model-computed significant wave height at stations #46070 and #46075.

Stations	Bias	Correlation coefficient	Slope	Intercept	STD	RMSE
46070	0.10	0.75	0.90	0.13	0.80	0.82
46075	0.19	0.91	0.90	0.03	0.51	0.56

Table 3
Bias, correlation coefficient, slope, intercept, standard derivation (STD) and root mean square error (RMSE) of the model-computed peak period at stations #46070 and #46075.

Stations	Bias	Correlation coefficient	Slope	Intercept	STD	RMSE
46070	1.0	0.28	0.31	5.47	2.19	2.78
46075	1.32	0.34	0.33	5.18	2.32	3.17

computed T_{peak} with respect to the observed T_{peak} has slopes of 0.31 and 0.33, with intercepts of 5.47 s and 5.18 s, and correlation coefficients of 0.28 and 0.34 at #46070 and #46075, respectively (Table 3). The bias was around 1.0–1.32 s, with RSMEs of 2.78 and 3.17 s, respectively.

Following the wave spectra partition method introduced by Hanson and Phillips (2001), Hanson et al. (2009) and Tolman and the WAVEWATCHIII®Development Group (2014), we also compared the simulated and observed significant wave heights of the windsea (SWHws) and swell (SWHsw) at station #46075 (Fig. 6). The correlation coefficients between model-simulated and observed SWHws values are shown to exceed 0.74. The model over-predicts the observed SWHws in the Bering Sea during the storm events in September–October, which is a key reason for a relatively large bias and RMSE reported in Table 4. The model is also reasonably capable of reproducing the SWHsw at this station (Fig. 6). In particular, it accurately reproduces the swell peaks in June and September, but underpredicts SWHsw in late October. Observed SWHsw values exhibit high-frequency variability, which appear to be smoothed out in the

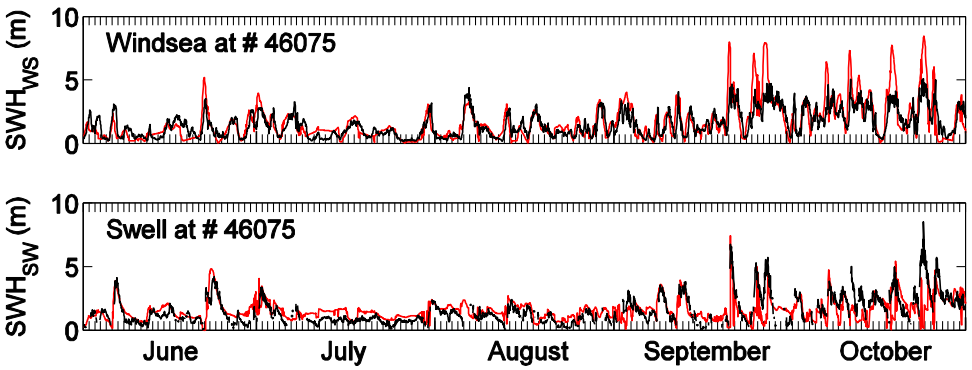

Fig. 6. Comparisons of model-computed (black curve line) and observed (red curve line) significant wind sea and swell heights at stations #46075 over the time period June–October, 2013.

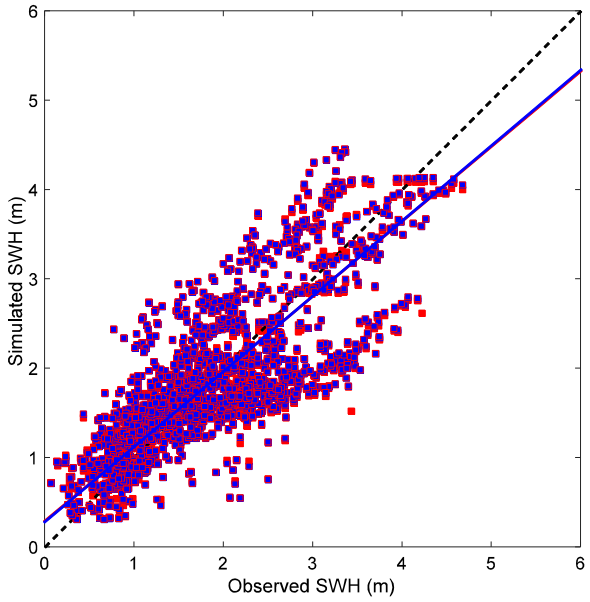

Fig. 7. Comparisons of model-computed and Jason-2 satellite-observed SWHs over the time period June–October, 2013, at latitudes over 55°N. Red and blue dots are simulation results for Case I and Case II, respectively.

Table 4
Bias, correlation coefficient and RMSE of model-computed wind sea and swell at station # 46075.

Stations	Wind sea			Swell		
	Bias	Correlation coefficient	RMSE	Bias	Correlation coefficient	RMSE
46075	0.35	0.74	1.10	0.23	0.65	0.90

simulated SWHsw. This is partially due to insufficient resolution in the wind forcing in time and space and intrinsic model biases, such as inadequacies in the basic source term physics in Eq. (2). These factors contribute to the relatively low correlation coefficients between model-simulated and observed SWHsw values (Table 4).

We also repeated the model-data comparison for Cases II and III without the inclusion of sea ice in the surface forcing, nor the ice-induced wave attenuation, and the results are mostly identical. The maximum difference in the SWHs between the cases with and without these sea ice formulations is less than 0.2 m, with an overall bias of <0.02 m. This is not surprising since these two stations were located around 55.08°N, which is outside of the 'permanent' ice coverage areas in the Arctic.

Additional comparisons were made with the Jason-2 satellite-derived SWH (hereafter referred to as SWH_{J2}) in the AO-SWAVE computational domain up to 66°N. The simulated SWHs for Cases I and II were interpolated to the sites with SWH_{J2} data. A scatter plot was created for the simulated SWH via SWH_{J2} in Fig. 7 with the statistics given in Table 5. In both cases, the correlation coefficients between SWH and SWH_{J2} are 0.77 and 0.78, with biases being close to zero and RMSEs of 0.55 m and 0.56 m, respectively. For Cases I and II, the linear regression function of computed SWHs with respect to observed SWH_{J2} has the same slope of 0.84 and intercepts of 0.29 m and 0.28 m. It is evident that neither the inclusion nor exclusion of ice-induced attenuation significantly affects the wave simulation results in the Pan-Arctic region, though the SWH tends to be underestimated in Case I and overestimated in Case II.

The disparities between model-simulated and observed values of SWHs, T_{peak}, SWH_{ws} and SWH_{sw} are caused by multiple issues associated with model physics, the inaccuracy of external forcing, and the parameterization of empirical model coefficients. The wind forcing used to drive the model was interpolated from the NCEP reanalysis product with a horizontal resolution of ~1.9 degree, which is not able to resolve the small to meso-scale spatial wind variability or short-term variability of the significant wave heights and frequencies observed on the buoys. Insufficient resolutions for wave frequency and directional domains may also cause errors in magnitude and direction of the group velocity and thus, the timing of the arrival of swells at observed stations. The simulation accuracy can be also significantly affected by the parameterizations used for S_{in}, particularly for the growth of the waves. These issues should be addressed in the future when AO-SWAVE is placed into operational forecasts.

3.2. Model-data comparisons at three stations in the Arctic Ocean

During the simulation period, only three stations (#48211, #48213 and #48214) on the northern coast of Alaska were available for comparison with model results. This coastal area is fully covered by ice during winter and spring of each year, and intermittently contains ice during early periods of the summers. The wave records at these three buoys started in July, after the area was free of ice.

To investigate the impact of the ice (in the interior Arctic Ocean) on the SWHs and T_{peak} at the three buoys on the Alaska shelf, we compared the model results with the buoy observations for Cases I, II and III. Taking SWH as an example, the model performance was assessed using the model skill coefficient (MSC) defined as

$$MSC = 1 - \frac{\sum_{i=1}^{i=N} \left(SWH_{m,i} - SWH_{o,i}\right)^2}{\sum_{i=1}^{i=N} \left(\left|SWH_{m,i} - \overline{SWH_o}\right| + \left|SWH_{o,i} - \overline{SWH_o}\right|\right)^2}, \quad (11)$$

where $SWH_{m,i}$ and $SWH_{o,i}$ are the model-simulated and observed SWHs, respectively; $\overline{SWH_o}$ is the mean value of $SWH_{o,i}$; N is the total number of

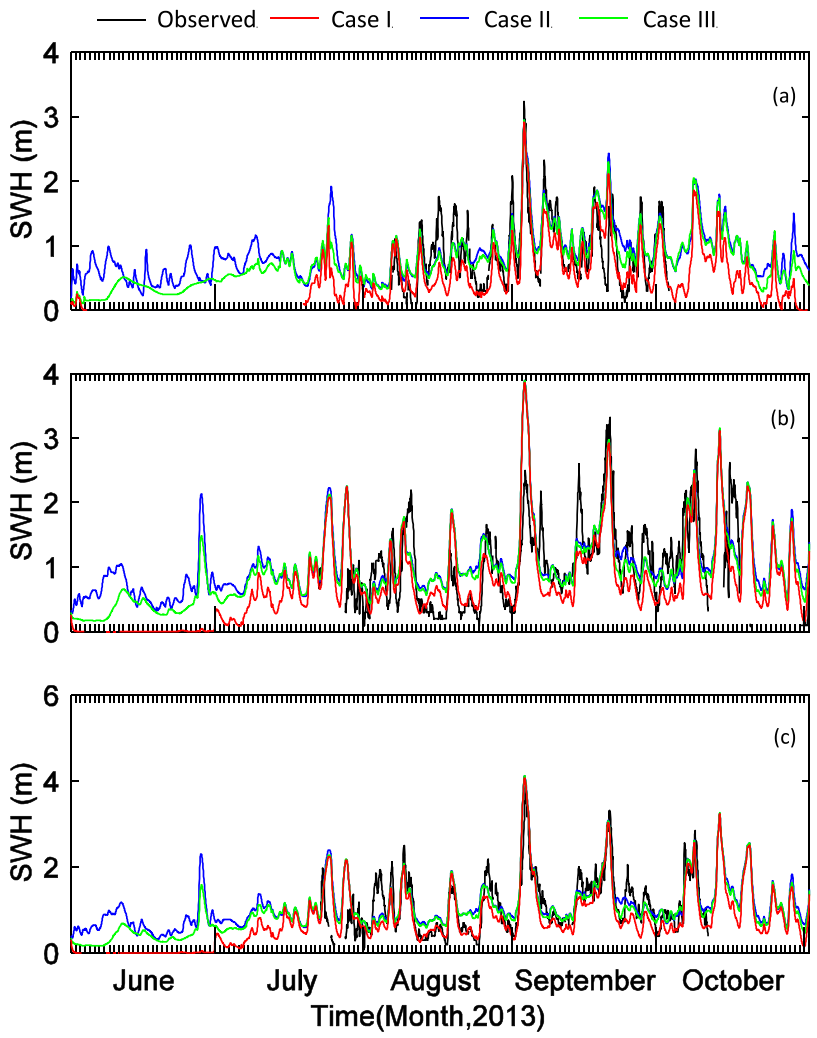

Fig. 8. Comparisons of model-computed and observed significant wave heights at stations #48211 (a), #48213 (b), and #48214 (c) over the time period June–October, 2013 for Cases I, II and III.

Table 5
Bias, correlation coefficient, slope, intercept, standard derivation (STD) and root mean square error (RMSE) of model-computed SWH for Case I and Case II.

Stations	Bias	Correlation coefficient	Slope	Intercept	STD	RMSE
Case I	−0.001	0.78	0.84	0.29	0.54	0.55
Case II	0.003	0.77	0.84	0.28	0.54	0.56

Table 6
Bias, correlation coefficient, RMSE and MSC of the model-computed significant wave height for Cases I, II and III at stations # 48211, #48213, and #48214.

Station IDs	Bias	Correlation coefficient	RMSE	MSC
Case I				
48211	−0.14	0.75	0.35	0.85
48213	−0.11	0.56	0.58	0.56
48214	−0.12	0.85	0.39	0.92
Case II				
48211	0.18	0.70	0.37	0.56
48213	0.14	0.55	0.56	0.33
48214	0.24	0.74	0.48	0.82
Case III				
48211	0.15	0.73	0.35	0.59
48213	0.11	0.55	0.56	0.37
48214	0.14	0.81	0.42	0.87

the measurements; and the subscript "i" is the ith measurement record. The performance is perfect when MSC = 1 but very poor when MSC = 0. Table 6 summarizes the MSC values for the three cases. The best is Case I, which takes into account the ice influence on surface forcing and ice-induced wave attenuation. The worst is Case II, which assumed ice-free conditions. Since the buoys were located in the ice-free area, the MSC difference is about 0.1–0.29 between Cases I and II, and about 0.05–0.26 between Cases I and III. A similar conclusion can be derived from comparisons of the correlation coefficients and RMSE (Table 6). Overall, Case I shows the best performance. SWH is overestimated in Case II and Case III and underestimated in Case I.

The performance of the AO-SWAVE for Cases I, II and III can also be viewed in the model-data comparison of the time series of SWH shown in Fig. 8. Over the period during which the observed SWHs are available, the model-computed SWHs for all three cases show similar performance levels at the crests but not at the troughs. Good model-data agreement is evident at the troughs in Case I, but the model-computed SWH is significantly higher than the observed data for Cases II and III. Although no wave data were recorded over the period from June to mid-July, the three buoy areas were intermittently covered by thin ice. As a result, the model-computed SWHs remain near zero for Case I. Ignoring either ice-induced wave attenuation or ice-reduced surface wind forcing (over the open ocean) can significantly overestimate SWH. At station #48211, the results for Cases II and III

Table 7
Bias, correlation coefficient RMSE and MSC of the model-computed peak period for Cases I, II and III at stations # 48211, #48213, and #48214.

Station IDs	Bias	Correlation coefficient	RMSE	MSC
Case I				
48211	−0.81	0.31	1.86	0.49
48213	−0.55	0.56	1.44	0.70
48214	−0.62	0.58	1.37	0.71
Case II				
48211	0.97	−0.10	2.68	0.30
48213	0.68	0.30	1.79	0.56
48214	0.55	0.26	1.80	0.54
Case III				
48211	1.30	−0.19	3.19	0.26
48213	0.73	0.15	2.09	0.49
48214	0.62	0.10	2.10	0.46

show relatively high values of SWH at levels >0.1 m, with maximum values up to ~1.2 m and 0.8 m, respectively. Similar evidence also occurs at stations #48213 and #48214. In late June, the model predicts a peak SWH at a level of ~0.3 m at stations #48213 and #48214 in Case I, but this peak is exaggerated by as much as to 2.0 m in Case II and 1.8 m in Case III.

We also compared model-simulated and observed peak periods at #48211, #48213 and #48214 for the three cases (Fig. 9), with the bias, correlation, RMSE and MSC shown in Table 7. The performance of Case I is much better than Cases II and III. Based on the absolute values of bias, RMSE and MSC, Case I is the best and Case III is the worst. At #48211, the correlation coefficient in Case I is 0.31, but is negative in Case II and Case III. Similarly, the MSC is remarkably higher in Case I than in Case II and Case III. At these three stations, over a certain time period, Cases II and III exhibit some unrealistic longer peak periods that were not evident in the observations; unrealistic peaks do not occur in Case I. It is clear that restricting the wind input and attenuation of swells to the ice-covered zone play a critical role in capturing the period of surface wave simulation at these three stations.

The comparison results are summarized using the Taylor diagrams shown in Fig. 10. As indicated by Tables 6 and 7, both correlation coefficients and RMSEs show that the Case I exhibited a better overall performance than Case-II and Case-III, especially for Tpeak. Fig. 10 shows that, compared with the standard deviation (STD) of observed SWH, Case 1 performs better than Cases II and III. For example, at #48211, the STD of the observed SWH is 0.50, and the STDs of model-simulated SWHs are 0.47, 0.41 and 0.40 respectively for Cases I, II and III.

3.3. Model-data comparisons with SWIFT buoys in the Arctic Ocean

Surface Wave Instrument Floats with Tracking (SWIFTs) were purposely designed to measure the wave fields in the Arctic Ocean. Wave data were collected by three SWIFTs in the Beaufort Sea in 2014 (Smith and Thomson, 2016). The drift tracks of these three SWIFTs are shown in Fig. 1 of Smith and Thomson (2016) and replotted as Fig. 11. The gray image over the sea is the ice concentration C_i on September 1, from daily SSM/I and SSMIS data. Compared with the fraction of sea ice cover (also is the ice concentration) in Fig. 1 of Smith and Thomson (2016), C_i was obviously high in the vicinity of 155°W 75°N. Both SWIFTs 10 and 11 were deployed on July 27 from the R/V Ukpik in the open ocean, and shared similar tracks until September 1, when SWIFT 10 traveled north and was trapped in the ice-covered sea until September 15, while SWIFT 11 drifted west. SWIFT 15 was deployed on August 5 in the partial ice cover and was caught in the MIZ until it was recovered.

These SWIFT data are used to validate the model results. Fig. 12(a–c) shows the time series of SWH recorded by SWIFT 10, 11 and 15 and the corresponding simulation results respectively, in which the ice induced wave attenuation is fully considered. Table 8 shows the performance of the model, compared with the SWIFT data.

Table 8
Bias, correlation coefficient, RMSE and MSC of model-computed significant wave heights at SWIFTs #10, #11 and #15.

SWIFT IDs	Bias	Correlation coefficient	RMSE	MSC
10	−0.02	0.66	0.57	0.82
11	−0.38	0.92	0.49	0.89
15	0.02	0.63	0.17	0.75

The red and black squares in Fig. 12(a–c) are the SWIFTs—recorded SWHs and the corresponding simulated SWHs, respectively, while the lines show the 9-day moving averages. From September 1 to September 15, SWIFT 10 was caught in the ice-covered sea but the daily SSM/I and SSMIS data did not show any ice along this track. Thus the simulation results show obvious overestimation during these 15 days. For the other days the moving average shows good agreement between simulation and observations, while the model underestimates SWH before August 8. SWIFT 11 drifted on an ice-free sea surface and the daily SSM/I and SSMIS data did not show any ice. Thus the model can accurately represent the SWH under these conditions, and the correlation coefficient and MSC are very high. The model also shows underestimation at high SWHs, but the overall performance is good. SWIFT 15 was deployed in the ice-covered sea and recorded the SWH in the MIZ. Fig. 12(d) shows the ice concentration during the track, according to the daily SSM/I and SSMIS data. The simulation results reproduced the trend of the SWH in the MIZ well, although the available observed SWH data from SWIFT 15 are scarce. On average, the simulation results underestimate SWH before August 10 and exhibit overestimations after this time. The trend is similar between simulation and observations and the parameters in Table 8 also show that the performance of the model is good.

The simulation results accurately met the observed SWH values along the track of SWIFT 11, because the ice concentration along the track is zero which corresponds well with the real ice state. When SWIFTs were trapped by ice, specifically, the whole track of SWIFT 15 and partial track of SWIFT 10, higher errors were experienced. However, the simulation results still conform to the observed data at SWIFT 10 and 15 well. The resolution and accuracy of the ice concentration is a key impact factor in the SWH simulations. Comparing Fig. 1 of Smith and Thomson (2016) and Fig. 11, there are obvious differences between the daily SSM/I and SSMIS sea ice data and the daily AMSR2 sea ice data; thus it is possible that inaccurate ice forcing and poor resolution of the ice fields are the main factors in the differences between model and observations.

4. Discussion

4.1. Impacts of ice-induced wave attenuation on wave generation and evolution

To evaluate the impact of ice-induced wave attenuation on wave generation and evolution in the ice-free coastal region, we selected station #48214 as a comparison site for the model-computed wave vector histories for Cases I, II and III over the period from July 6 to July 19, during which this location was intermittently covered by sea ice. The analysis was done for both windsea and swell (Fig. 13).

Buoy #48214 was dominated by weak southerly winds during July 6, northeasterly winds with a maximum speed of ~9.3 m/s during July 7–11, and then south-southeasterly winds with a maximum speed of ~8.3 m/s during July 12–19 (Fig. 13a). This site was within the marginal ice zone during July 7–14, but remained ice-free after July 15 (Fig. 13b). Ice coverage attenuated the wave energy and reduced the energy of wind forcing over the ocean, and thus directly influenced

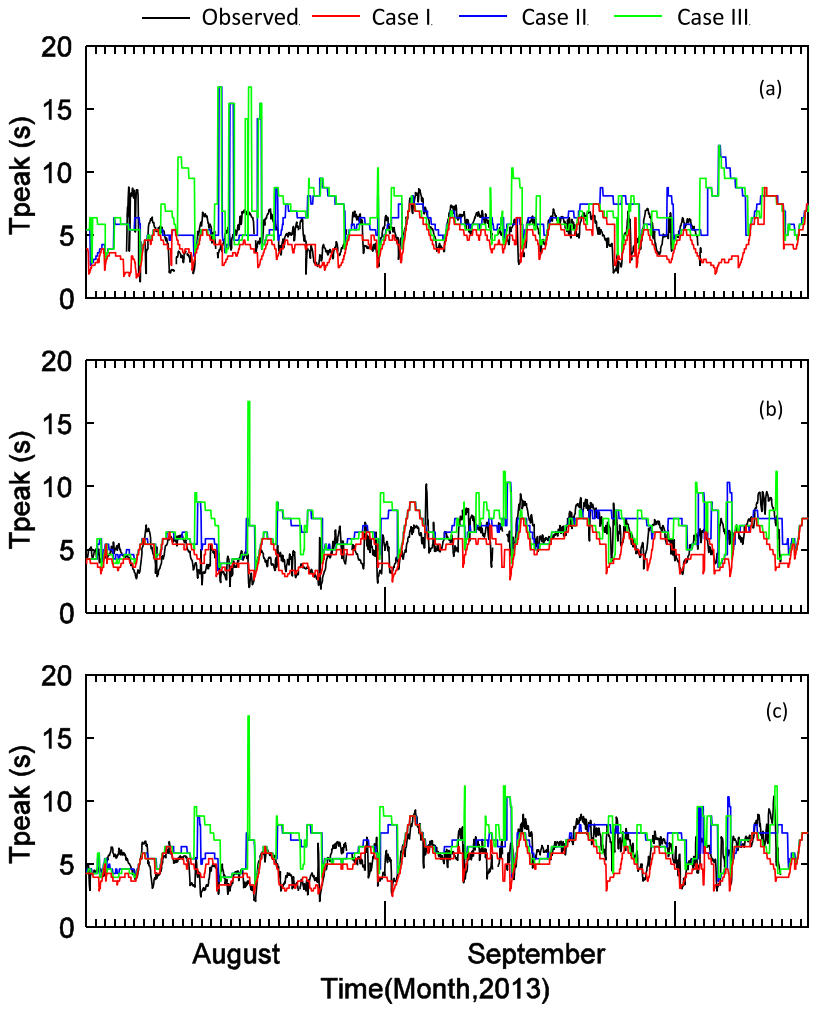

Fig. 9. Comparisons of model-computed and observed peak periods at stations #48211 (a), #48213 (b), and #48214 (c) over the time period August–October, 2013 for Cases I, II and III.

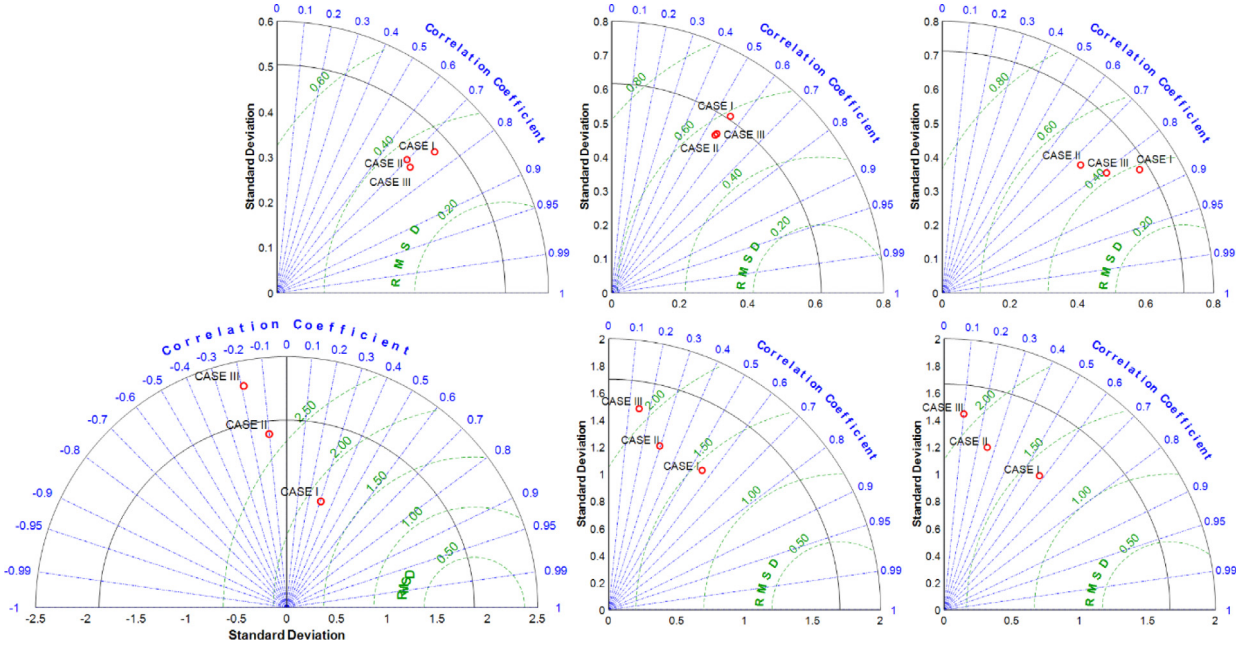

Fig. 10. The Taylor diagrams of SWH (upper three panels) and Tpeak (lower three panels) for station (a)(d)#48211, (b)(e) #48213, and (c)(f) #48214.

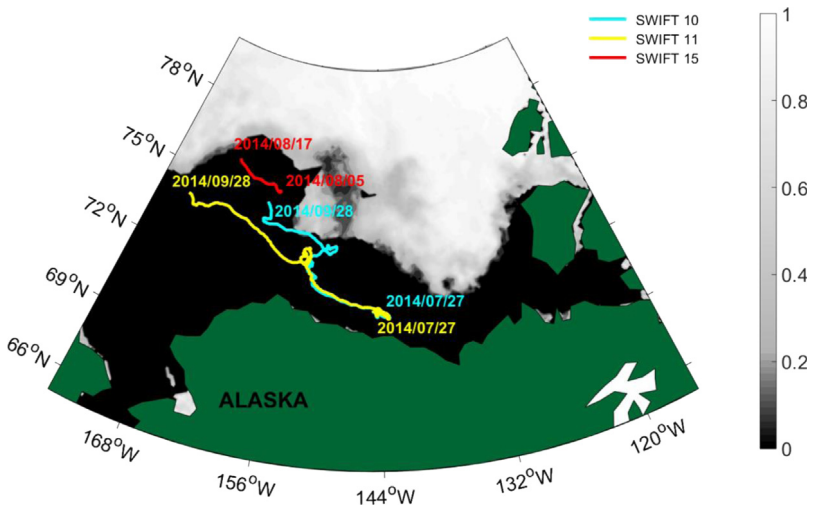

Fig. 11. The tracks of SWIFTs 10 (blue), 11 (yellow), and 15 (red). The deployment and end dates of the SWIFTs are marked at the beginning and the end of the tracks. The ice concentration is shown by the gray level, from the SSM/I and SSMIS data.

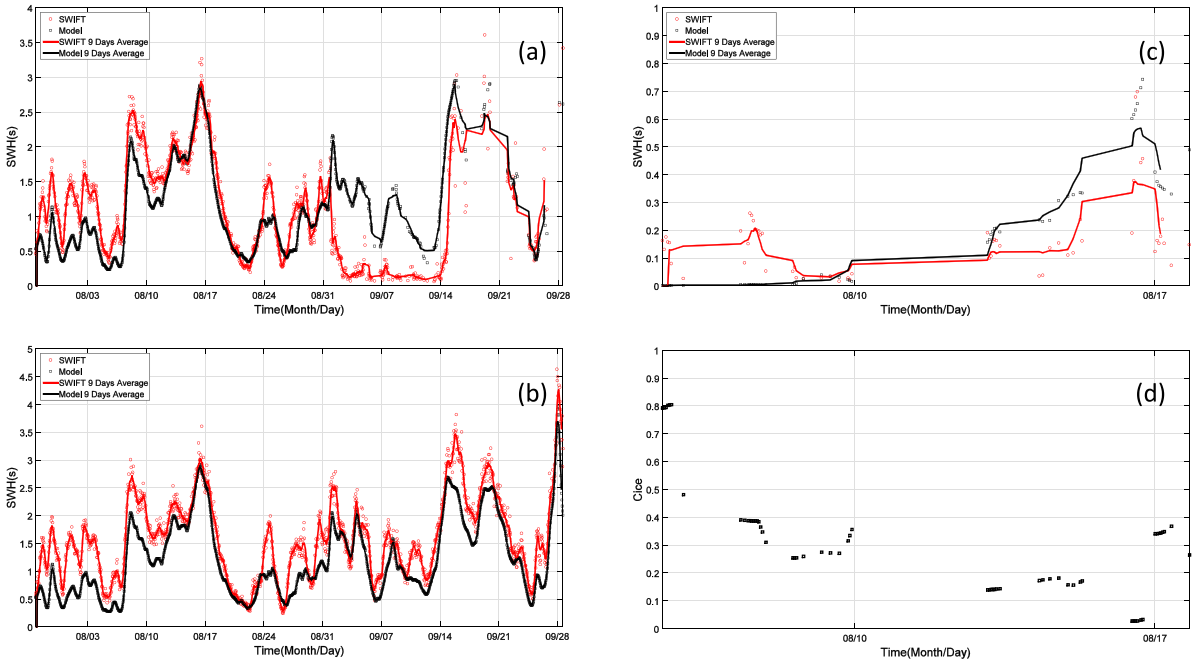

Fig. 12. Comparisons of model-computed and observed significant wave heights at SWIFTs (a) #10, (b) #11, and (c) #15, and (d) the ice concentration at SWIFT #15, from the SSM/I and SSMIS data.

the windsea generation and evolution for Case I (Fig. 13c). In this case, the wind waves were generated on July 7 when the ice concentration was 0.15. After generation, during its development period, the wave energy gradually downshifted from high to low frequencies and then rapidly dissipated when the ice concentration increased to 0.24 on July 8. The windsea was regenerated again when the ice concentration dropped to 0.16 on July 9 and experienced additional high-to-low frequency downshifting during its evolution until July 10. During this period, the ice concentration increased to 0.5. Such variability in the windsea energy continued until the site became ice-free on July 13. After that, the windsea followed a regular growth pattern. In the MIZ, the model results suggest that the energy dissipation of the windsea was generally accompanied by an apparent frequency increase as the ice concentration increased. Actual shifting of the spectral peak frequency occurred as the result of nonlinear wave–wave interactions, which were originally elucidated by Hasselmann (1962) and verified by the JONSWAP experiment of Hasselmann et al. (1973). Relatively low ice concentrations appear to result in an upshift of the energy spectra, because the ice-induced wave attenuation is apparently more effective at higher frequencies than at lower frequencies.

In Case II, without the ice-induced wave attenuation and the blocking effect of the ice on the open ocean surface forcing, the model-computed windsea is just a result of normal wind generation (Fig. 13d). A northeasterly windsea developed when the northeasterly wind appeared on July 7. During the wave evolution period, the energy of this windsea increased when the wind speed became strong and its frequency shifted from high to low. The windsea grew steadily as the northeasterly wind continued for 5 days, reaching a relatively stable peak period of 5 s after July 10.

Case III considered the blocking effect of the ice on the open ocean surface forcing but not the ice-induced wave attenuation. Thus, although the development of the windsea was quite similar to that observed in Case I, the wave energy reached higher values at a lower peak frequency. As the ice concentration increased, the change in

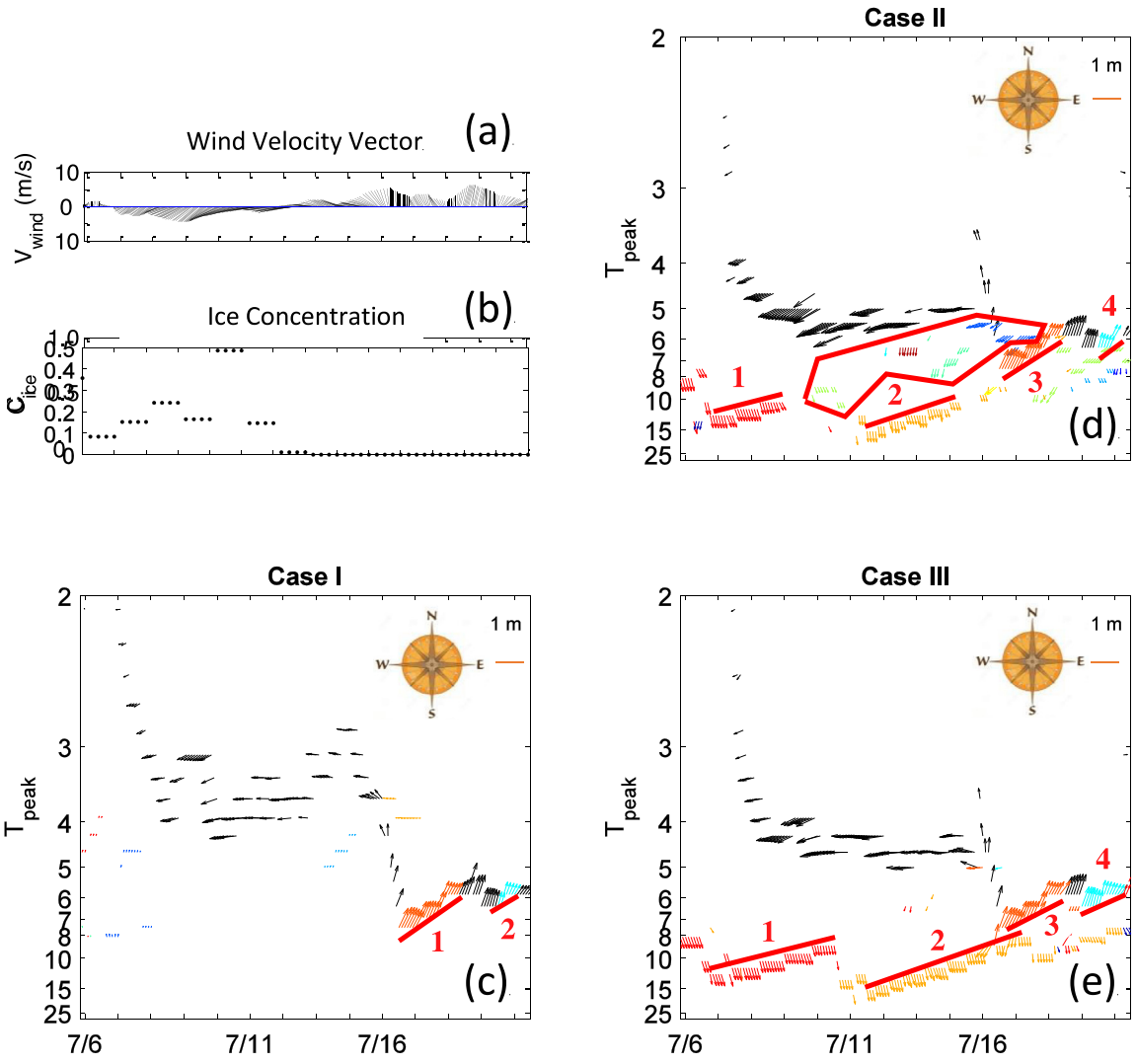

Fig. 13. Left-top two panels: (a) the time series of the wind velocity vector (m/s) and (b) ice concentration at the station #48214 over the time period July 6–19, 2013. The other three panels: the vectors of wind sea and preliminary swell groups at the station #48214 over the same period for (c) Case I, (d) Case II, and (e) Case III. The ice concentration was recorded every 6 h. The vertical red vector inside each figure indicates the magnitude of 1-m SWH. The azimuth represents the windsea and swell frequencies, respectively. The direction and length of the vectors indicate the propagation direction and significant wave height. Black vectors refer to windsea, while adjacent vectors with other same colors refer to a swell group.

frequency was not as remarkable as that in Case I (Fig. 13e). The energy of this windsea was, at most, about 3 times higher than that of Case I, and it developed even when the ice concentration dropped to zero. These features were more evident later in time, suggesting that the ice-induced wave attenuation played a key role in the wave dissipation and the apparent downshifting of the peak frequency in Case II. By comparison, in Case III, only nonlinear wave–wave interactions affected the downshifting of the peak frequency energy. Therefore, the process occurred at an apparently slower rate.

Development and evolution of swell waves significantly differed among the three cases, with and without inclusion of the ice. The number and intensity of these swell groups are considerably distinct. In Case I, before July 15, no remarkable swell groups were detected at station #48124, but some swells with very small amplitudes occurred over the periods of July 6–7 and July 13–14, respectively (Fig. 13c). Although the amplitudes were of the order of 0.01 m, the characteristics of the swell groups and frequency upshift were still visible. These tiny swells were the products of ice-induced wave attenuation. After July 12, the ice completely disappeared, and the site was dominated by two groups of swells (Groups I-1 and I-2), which propagated northeastward with amplitudes of ~0.6 m and periods of 6–8 s

When the ice-induced wave attenuation and the blocking effect of the ice on the ocean surface forcing were removed, the location exhibited different types of swells at all times (Fig. 13d). During the first four days, one group of swells was detected (Group II-1), which propagated southward with an amplitude of ~0.6 m and periods of 10 ~ 15 s After July 10, several groups of swells were found, which mainly propagated southward with amplitudes of 0.05–1.0 m and periods of 5–10 s There are too many wave groups to be individually analyzed. Among them, Groups II-2, II-3 and II-4 in Case II were also clearly detected as Groups III-2, III-3 and III-4 in Case III. If the blocking effect of the ice on the ocean surface wind forcing was considered, but not ice-induced wave attenuation (Case III), some swell groups in Case II either disappeared or weakened (swells inside the red polygon). During the first five days, in Case III, the site was dominated by one group of the southward-propagating swells (Group III-1) with an amplitude of about ~0.55 m and periods of ~10 s Group III-1 corresponded to Groups II-1. After July 11, three distinct groups of swells were detected. Groups III-3 and III-4 are the same as Groups I-1 and I-2 in Case I. Groups II-3 and II-4 in Case II traveled from the southwest. Group III-2 was identified in both Case II and Case III, though in Case II it was partially lost because the spectrum had too many other interacting energy components. This swell group (Group II-2 and Group III-2) may

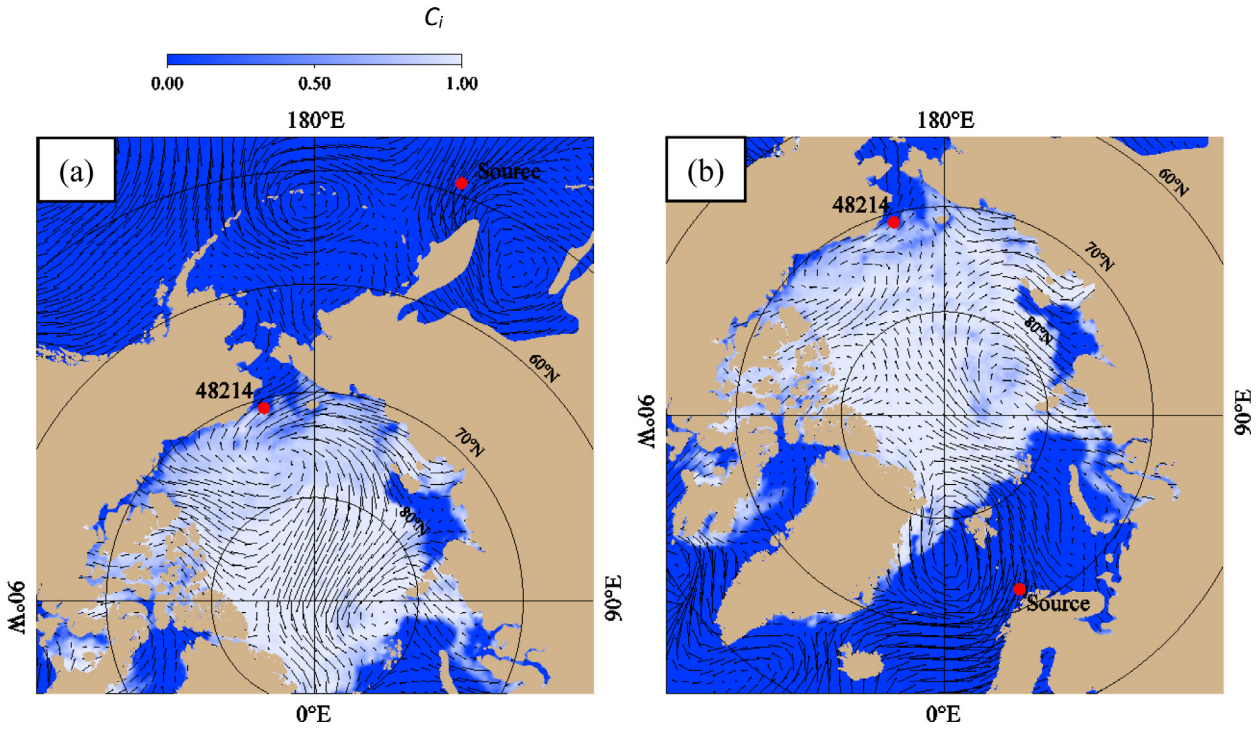

Fig. 14. Illustration of the original of the swell groups that were observed at station #48214 over the periods July 15–17, 2013 for Case I (a) and July 13–16, 2013 for Case III (b). The colors refer to the ice concentration, while the vectors refer to the wind field when the swells are generated at the location of "Source".

correspond to the tiny swells during the period of July 10–12 in Case I, which was effectively attenuated by the ice cover. In summary, swells from the ice-free ocean area in the southern region of the domain were detected in all three cases. Case III removed swells that were generated in the ice-covered area in Case II (the complicated swell groups in the red polygon in Case II). In addition, Case I attenuated swells that were either generated in the ice-covered area or traveled though the ice-covered sea (Groups III-1 and III-2).

We used a swell-tracking method (Hanson and Phillips, 2001) (described in Appendix B) to locate the generation location and time of Group I-1 for Case I and Group III-2 for Case III. Group I-1 was detected at station #48214 during the period July 15–17. The original source of this swell group is shown in Fig. 14a, indicating that this swell group was generated at 18:00:00, July 9. A persistent wind field in the Northwest Pacific Ocean with a speed of >10 m/s developed a robust swell group, which traveled through Bering Strait and reached station #48214. Group III-2 was originally generated in the ice-free area of the Arctic Ocean around 10:00:00, July 7 and traveled through the ice-covered area to reach station #48214 (Fig. 14b). This swell group represents an artificial result because the effect of the ice-induced wave attenuation was ignored in the Case III wave simulation.

4.2. An 'ice retreat-wave growth' positive feedback mechanism

In our study, implementing wave-induced attenuation allowed the wave energy to propagate into the MIZ and the ice-covered area. As the ice concentration increased and the waves encountered more ice floes, the wave energy rapidly dissipated as its travel increasing distances into the MIZ increased. Since short waves attenuated more rapidly than long waves, as the waves propagated deeper into the MIZ, the peak of the wave energy tended to shift to lower frequencies in the energy spectrum. Under conditions where the daily ice fields are derived from remote sensing data and the wave field is from simulation results, an 'ice retreat-wave growth' positive feedback mechanism can be further proposed and analyzed. The ice-free sea surface area increases with the retreating ice, which directly promotes the waves' growth. In turn, wave dissipation can induce ice floe breakage, and thus accelerate the melting of ice and thus, the retreat of the ice. Here, a brief discussion is given on (a) the impacts of the ice retreat on wave growth and ice breakage and (b) the influence of ice breakage on ice melting.

4.2.1. Impacts of ice retreat on wave growth and ice breakage

Williams et al. (2013a) introduced a method to estimate the conditions whereby the waves in the MIZ can break ice floes. The basic idea is to compare the significant strain amplitude (E_s) for the ice floes, with the critical breaking strain (ε_c) through a criterion given as

$$E_s > E_c = \varepsilon_c \sqrt{\frac{-2}{\log(P_c)}}, \tag{12}$$

where E_c is the critical significant strain amplitude and P_c is the probability criterion specified as $P_c = e^{-2} \approx 0.14$. ε_c is given as

$$\varepsilon_c = \frac{\sigma_c}{Y^*}, \tag{13}$$

where Y^* is the strain modulus equaling

$$Y^* = Y_0 (1 - 3.51 v_b) - 1 \text{ GPa}, \tag{14}$$

with $Y_0 = 10$ GPa, and σ_c is the flexural strength, equaling to

$$\sigma_c = \sigma_0 \exp\left(-5.88\sqrt{v_b}\right), \tag{15}$$

where v_b is the brine volume and σ_0 is a constant specified as 1.76 MPa. In our experiments, v_b is assumed to be 0.1.

In our approach, E_s was calculated from SWH and T_{peak} was deduced from the wave spectrum. Assuming that ice breakage events happen in the direction of the highest wave energy (θ_m) and only the wave energy within the direction segment $|\theta_m - \theta| < \frac{\pi}{2}$ contribute to ice breaking, we can calculate E_s by

$$E_s = 2\sqrt{\int_{\theta_m - \frac{\pi}{2}}^{\theta_m + \frac{\pi}{2}} \int_{0.04}^{1} S(\omega, \theta) \cos(\theta_m - \theta) \left(\frac{h}{2} k_{ice}^3 \frac{|\Gamma|}{k}\right) d\omega d\theta}, \tag{16}$$

where h is the thickness of the ice floe; Γ (= 0.8) is the transmission coefficient for waves traveling from the water into the ice; ω is the

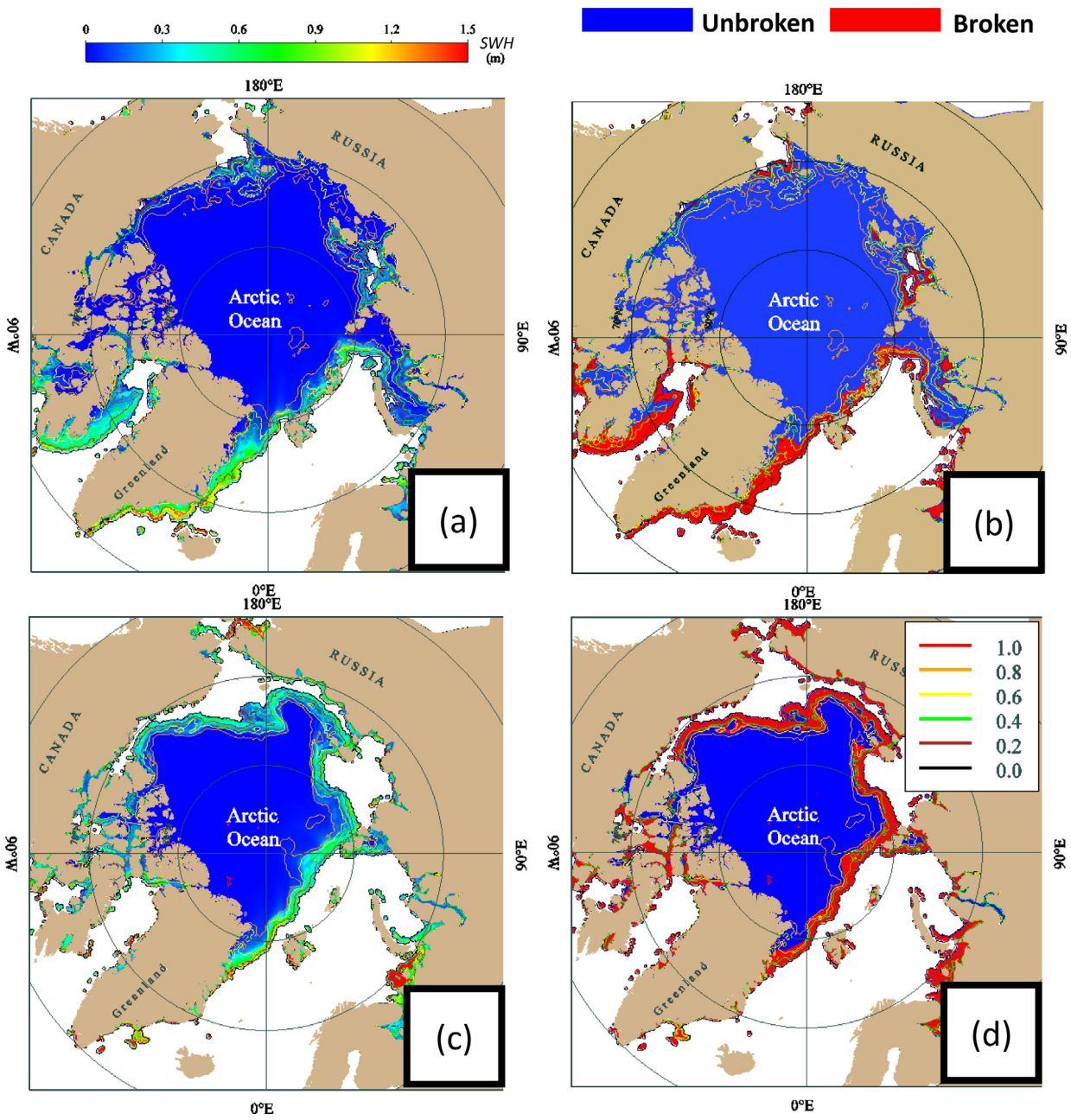

Fig. 15. Distributions of the monthly-averaged significant wave height (left two panels) and wave-induced ice breakage area (right two panels), for the month of July (top two panels) and September (lower two panels) in the Arctic Ocean and adjacent Pacific and Atlantic Oceans in 2013. The model results used here were from Case-I. The lines in each figure are the ice concentration contours from 0 to 1 with intervals of 0.2 (legend in (d)).

angular frequency; k is the wave number; k_{ice} is the wave number of the ice plate and is taken as the positive real root as given by Williams et al. (2013a), specifically their Eq. A.7.

Following Eqs. (12)–(16), we can estimate the average value of E_s in the Arctic Ocean; as examples, the results for July and September 2013 are represented in Fig. 15. In July, the significant ice breakage was mainly located within the MIZ on the North Atlantic side of the Arctic Ocean, where the breaking event can occur in the area with ice concentration C_i being up to 0.6 (Fig. 15: upper panels). Although most of the entire Arctic Ocean was still covered by sea ice, it did have ice-free areas in the Chukchi Sea and Laptev Sea, and ice breakage occurred in these two regions. By September, a large portion of the Arctic had become ice-free, providing potentially long fetch conditions for wave generation and growth. The ice breakage area in the Chukchi and Laptev Seas became larger and extended to the Beaufort Sea and East Siberian Sea. With rapid ice melting, the MIZ on the Atlantic side retreated toward the Arctic, accompanied by an intensification of ice breakage (Fig. 15: lower panels).

In order to quantify the influence of the ice retreat on wave growth and ice breakage, we divided the Arctic Ocean region with latitudes ≥ 66°N into three sector zones: Sector I: 30°W–90°E; Sector II: 90°E–180°E; and Sector III: 120°W–180°W (Fig. 1). For simplicity, Sectors I, II, III are hereafter referred to as S-I, S-II and S-III, respectively. In each sector, we estimated the ratios of the open-water area (Ω_{free}) and ice breakage area (Ω_{break}) to the total sector area (Ω_s) (Fig. 16a–c). Hereafter, we defined these two ratios as $r_{free} = \frac{\Omega_{free}}{\Omega_s}$ and $r_{break} = \frac{\Omega_{break}}{\Omega_s}$. We also calculated the averaged SWH and T_{peak} in the open water in each sector and related them to the percentages of ice-free and ice breakage areas (Fig. 16d–f). The imaginary lines refer to the variation trend of SWH or T_{peak} before or after Ω_{free} reaches the peak values.

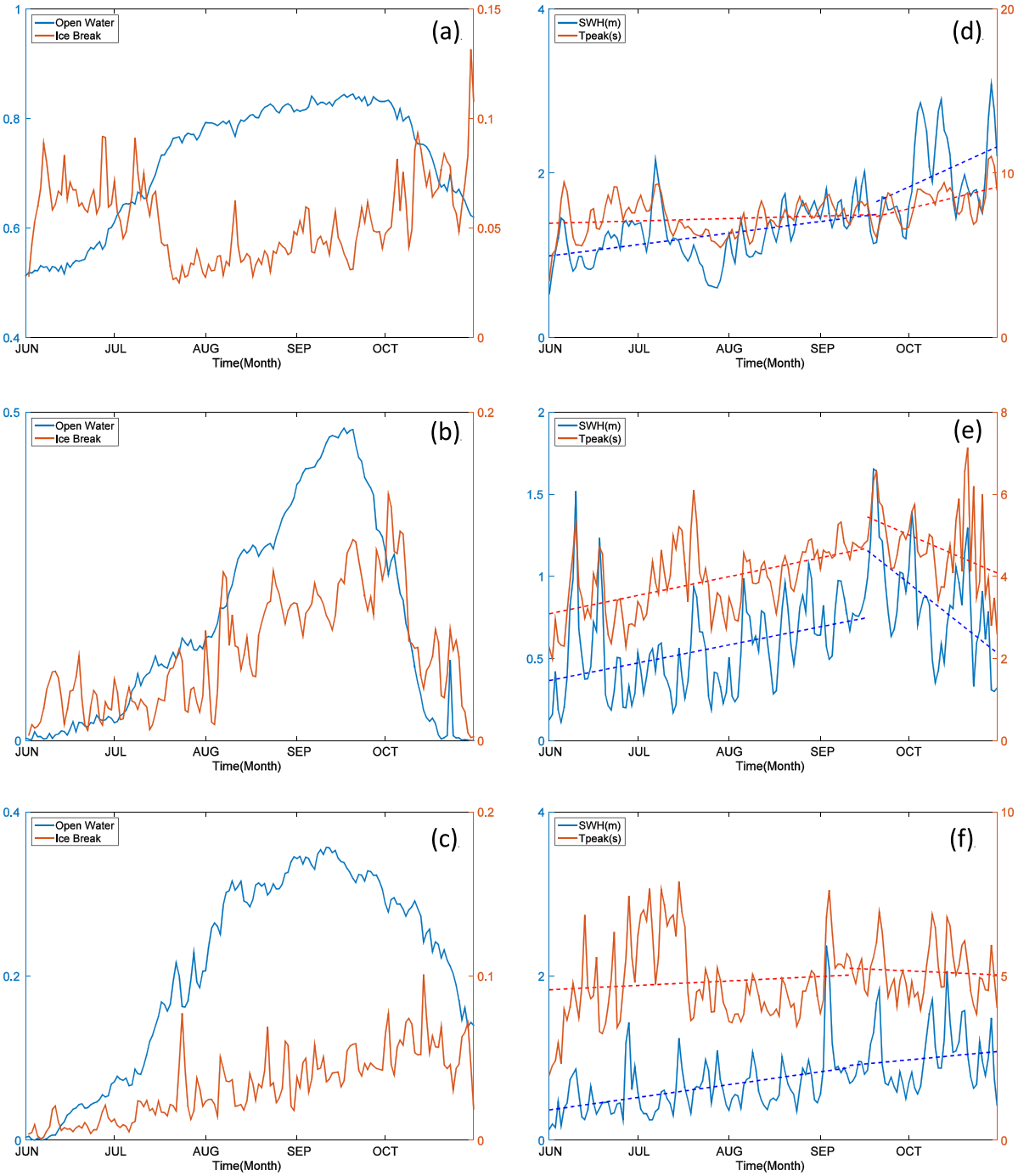

Fig. 16. Changes in the area of open sea (blue lines in left two panels), area of ice breakage (red lines in left two panels), SWH (blue lines in right two panels) and Tpeak (red lines in right two panels) versus time for the spatial scale covering section 1 (upper two panels), section 2 (middle two panels), and section 3 (lower two panels) over the time period June–October, 2013.

The responses of r_{break} to change in r_{free} differed significantly in these three sectors. In S-I (Fig. 16a), r_{free} increased from 0.51 to 0.84 during the time period June 1–September 20. However, r_{break} did not follow the change in the ice-free area, oscillating around 0.06 during June–early July, dropping to around 0.03 in mid-July, and then varying around 0.03–0.06 until late September. After September 20, the ice formation caused r_{free} to start to decrease, but r_{break} did not drop. Instead, it showed an increase. In S-II (Fig. 16b), r_{break} generally followed the same growth and decline trends as r_{free}, although with a 0.5-month time delay. r_{break} increased from nearly 0 to 0.15 as r_{free} grew from nearly 0 to 0.48 over the period June–early October. It then rapidly decreased toward 0 as r_{free} dropped to 0 over the October period. In S-III (Fig. 16c), r_{break} showed an obvious increasing trend during both the increasing phase and the early decreasing phase of r_{free}, except in late October when r_{break} began to decrease.

Theoretically speaking, wind-generated wave growth is the consequence of ice retreat and the increase of open water, which is also the reason for increased ice breakage area. In S-I, the linear regression lines of SWH and T_{peak} suggest that regardless of how the period of r_{free} increased or decreased, both amplitudes and periods of the surface waves show overall increasing trends during the June–October period. The rates of increase exhibited two time phases: the first is a gradual increase during the r_{free} increasing period and the second, a rapid increase during the r_{free} decreasing period. In this sector, changes in

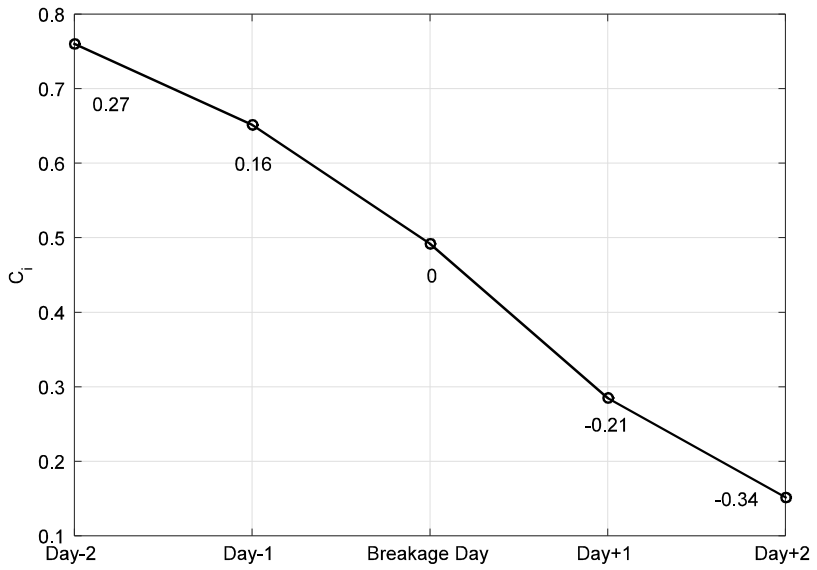

Fig. 17. The averaged ice concentration within 5 days of the breakage events. The numbers are the ice concentration difference compared with C_i on the ice breakage day.

r_{break} follow changes in SWH and T_{peak}, but do not directly correlate with the change in r_{free}. In S-III, the increase of r_{break} follows change in SWH rather than change in r_{free}. In S-II, changes in SWH and T_{peak} share the same trend as r_{free}, and therefore change in r_{break} follows change in r_{free}.

From June through October, on the Atlantic side of the Arctic Ocean (S-I), because r_{free} remains above 0.5, it is clear that fetch does not restrict wave growth. Therefore, wave–ice interactions can remain active and are limited by the wind field over the time period from June to October. On the Pacific side of Arctic Ocean (S-III), the fetch is a critical limit on wave growth. For surface waves, SWH can increase with increasing fetch and during the early ice formation period. As r_{free} kept decreasing, toward the end of October, SWH generally decreased and r_{break} dropped rapidly to 0.02 while r_{free} decreased to 0.14. S-II is geographically between S-I and S-III, where fetch plays a critical role in limiting wave growth. In this region, the temporal change in r_{break} is directly correlated with variability in r_{free}.

4.2.2. *Influence of ice breakage on ice melting*

We evaluate the influence of ice breakage on ice melting by examining the change in ice concentration (C_i) before and after the occurrence of breakage events. During this study, C_i was limited to be within the range of 0.4–0.6 when ice breakage occurred. The averaged anomaly value for C_i over a 5-day period is calculated and shown in Fig. 17, which includes the day when the ice breakage occurred plus two days before and after. Using the ice breakage day as a reference, the difference in C_i relative to that day was 0.16 and −0.21, one day before and after the occurrence of the ice breakage event, respectively. This implies ~31% increase in the ice melting rate after the breaking of the ice. Over a 2-day period, the differences are 0.27 and −0.34, indicating an average rate increase of ~26%. By contrast, the ice melting rate, after C_i reaches the range 0.4–0.6, does not accelerate if there is no ice breakage. This estimate suggests that ice breakage can accelerate the ice-melting rate through a positive feedback process.

4.3. *Advantage of the improved algorithm to estimate* $S_{att,ice}$

In Section 2, we introduced a new algorithm to improve the estimation of $S_{att,ice}$. To evaluate this new method, we compare the monthly averaged values for SWH and Ω_{break} between the traditional and improved algorithms described in Eqs. (3) and (9). For the sake of discussion, we denote the traditional and improved wave-induced attenuation algorithms as "T_{WA}" and "I_{WA}". For example, Fig. 18 shows the monthly average values for SWH, and Ω_{break} obtained from T_{WA} for September 2013, and the differences in the results obtained from I_{WA}. Compared with the results shown in Fig. 15, the T_{WA} approach produces higher values for SWH and deeper penetrating areas into the MIZ, especially on the Atlantic side (Fig. 18a). The differences are mostly located within the MIZ where the ice concentration was higher than 0.6. The T_{WA} results indicate that SWH can even reach 0.2 m in regions where the latitude is higher than 85°N and where the ice concentration is higher than 0.8. Given that the ice concentration was close to 1, it is unreasonable for the wave energy to still be noteworthy.

Based on the field measurement data, Kohout et al. (2014) estimated the decay rate for waves, SWH, to be -1.07×10^{-6} m^{-1} after the surface waves penetrated into the MIZ, when SWH = 0.2 m. We also estimated the decay rate for SWH from T_{WA} and I_{WA}, respectively, by measuring the distance, over which SWH decayed from 0.2 m to 0.1 m, in the direction of the wave energy propagation. These results are -4×10^{-7} m^{-1} for T_{WA} and -1.13×10^{-6} m^{-1} for I_{WA}. The decay rate derived from T_{WA} was significantly lower than that derived from the field measurements. This implies that, given the same amplitude of SWH, then T_{WA} requires more than twice the distance to attenuate the wave energy. It is clear that T_{WA} can significantly overestimate the wave penetration distance into the MIZ. The decay rate derived from I_{WA} is of the same order of magnitude as that derived from the field measurement data.

Further comparisons were made for the change of temporally and spatially averaged SWH, T_{peak} and E_s over the entire simulation period and the ice-covered region with respect to ice concentrations, in increments of $0.1C_i$ (Fig. 19). As C_i increases, SWH decreases faster for T_{WA} than for I_{WA}. Similarly, T_{peak} showed a higher rate of increase for I_{WA} than for the T_{WA} case. Correspondingly, E_s showed a faster decay for I_{WA} than for the T_{WA} case. On average, ice breakage does not happen when $C_i \geq 0.4$ in the I_{WA} case, but persists until C_i reaches 0.55 for the T_{WA} case.

5. Summary and conclusions

FVCOM-SWAVE was modified by (a) the inclusion of a parameterization for ice-induced wave attenuation with a newly designed dissipation term in the wave spectral action balance equation and (b) the development and implementation of a coordinate projection method for sea surface wave simulation at high latitudes. This modified version of the unstructured-grid surface wave model was configured within the Global-FVCOM grid to examine the influence of ice-induced

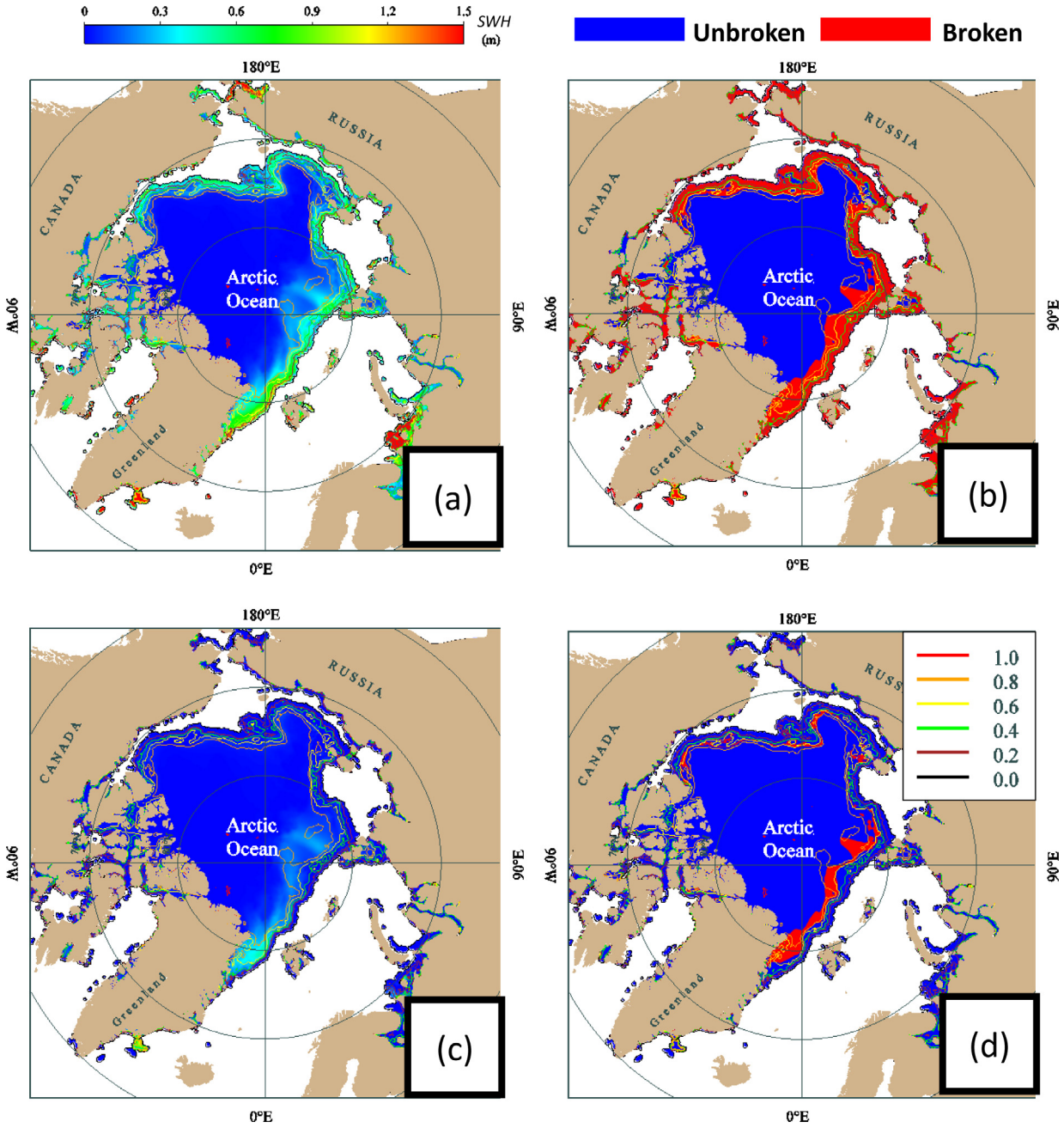

Fig. 18. Distributions of the monthly-averaged (a) significant wave height, (b) wave-induced ice breakage area, simulated based on the TSTS model, and the differences between the simulation results of (c) SWH and (d) breakage area from TSTS model and NSTS model, in the Arctic Ocean and adjacent Pacific and Atlantic Oceans for September, 2013. The model results used here were from Case-I. The lines in each figure are the ice concentration contours from 0 to 1 with intervals of 0.2 (legend in (d)).

wave attenuation on waves (windsea and swells) propagating into and out of the MIZ in the Arctic Ocean. Numerical experiments were carried out for three cases to estimate the effect of the inclusion of the ice-induced wave attenuation on the wave simulations and the blocking effect of the ice on ocean surface forcing.

We found that simulation results improved when the ice-induced attenuation and the blocking effect of the ice on the surface forcing mechanisms were included in the model system for simulating surface waves. The Global-FVCOM model is capable of reproducing the wave evolution trend in the Arctic Ocean, both in open waters and ice-covered areas. In particular, the process-oriented experiment suggests that the ice-induced wave attenuation plays a key role in the dissipation of windsea and swell waves in the ice-covered region. Ignoring this process can lead to biases in simulations of both windsea and swells. The new wave attenuation algorithm introduced in our study, which takes into account the grid-dependent numerical dissipation error, can provide more realistic estimates of wave attenuation in the MIZ and in the ice breakage area.

Using simulated wave spectra, an empirical method derived by Williams et al. (2013a) was introduced to estimate the probability for wave-induced ice breakage in the MIZ. The results show that wave-induced ice breakage mostly occurs in regions where ice concentration is lower than 0.4. In this study, we examined the importance of fetch on wave–ice interactions and its relationship with wave field and ice breakage. We found that the wind-generated wave growth is limited by fetch, as found in pioneering field experiments like JONSWAP by Hasselmann et al. (1973) and numerous efforts since that time, especially in Sectors II and III. Wave-induced ice breakage consistently occurs more frequently on the Atlantic side of the Arctic Ocean because the vast expanse of open water in the North Atlantic provides essentially

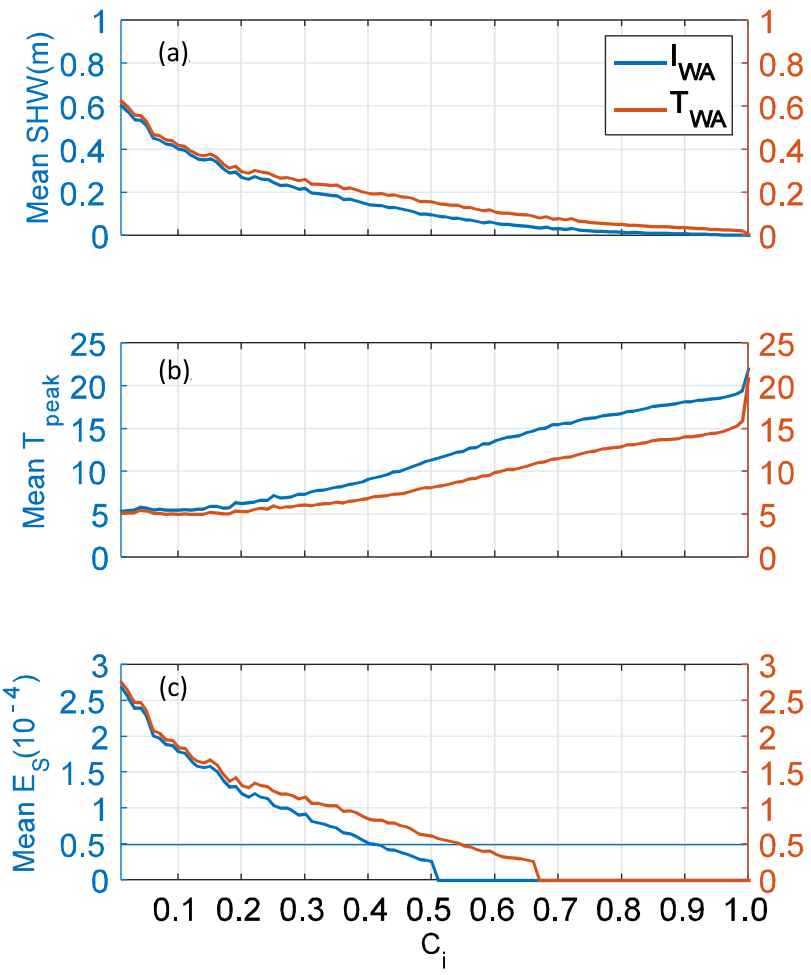

Fig. 19. Changes of the average significant wave height (a), peak period (b) and significant strain amplitude (c) versus the ice concentration estimated for the spatial scale covering the entire Arctic Ocean over the time period June–October, 2013. The average was done for every 0.01 ice concentration interval. The horizontal line in (c) refers to the critical strain amplitude.

'unlimited' fetch conditions for wave generation. On the Pacific side of Arctic, although the fetch limits wave growth, the magnitude of the surface waves can still intensify during the ice formation period, and thus the wave–ice interactions can be active until the middle of October when wave energy and ice breakage are both limited by fetch. Inside the Arctic Ocean, particularly in the region between 90°E and 180°E, fetch plays a critical role in limiting wave growth. In this region, the temporal change of the ice breakage area is directly correlated with the variability of the open water area. The notable difference between the ice melting rates before or after the ice breakage events suggests that ice breakage has a positive impact on ice melting, which supports the "ice retreat-wave growth" positive feedback mechanism.

Acknowledgments

This work was supported by the National Natural Science Foundation of China under Grant Number 41606208, Global Change Research Program of China (2015CB953900) and the postdoctoral research fund of the International Center for Marine Studies (ICMS) at Shanghai Ocean University (SHOU), China for Yang Zhang and by National Science Foundation (NSF), USA grants OCE-1203393, OCE-109341 and PLR-1603000 for Dr. C. Chen and his coworkers at UMASSD team and PLR-1203643 for Dr. R. C. Beardsley. The FVCOM-SWAVE system was developed with infrastructure support by the Sino-US Joint Innovative Center for Polar Ocean Research (SU-JICPOR), ICMS/SHOU. G. Gao was supported by the National Natural Science Foundation of China under Grant Number 41276197, the Global Change Research Program of China (2015CB953900), Shanghai Eastern Scholar Program, China under Grant Number No. 2012-58, and Shanghai Shuguang Program, China. Yu Zhang was support by the National Natural Science Foundation of China under Grant Number 41706210. For Arctic studies, W. Perrie was supported by the US Office of Naval Research for the Sea State Boundary Layer Project (N00014-15-1-2611), the Canadian Office of Energy R & D, Canada, the Belmont Foundation, USA and the Canadian Natural Science and Engineering Research Council, and the Canadian Space Agency.

The FVCOM version 4.0, which solved the coordinate system mismatch at high latitudes and the North Pole singularity problem, can be downloaded from the official website of FVCOM (http://fvcom.smast.umassd.edu). All the data we used in this paper and the simulated Global-scale wave data and significant strain amplitude of ice can be obtained from Yang Zhang (email: yzhang@sio.org.cn).

Appendix A. Treatment of meridian convergence and North Pole singularity

In SWAVE, the spectral wave energy is calculated as a matrix composed of the sum of the energy segments for each frequency and direction. This was done by the conservation equation for spectral action density, used in modern state-of-art third generation wave models (WWIII and SWAN) (Booij et al., 1999; Tolman et al., 2002; Tolman, 2009; Tolman and the WAVEWATCHIII®Development Group, 2014; Qi et al., 2009; Bidlot, 2012). Following WWIII and SWAN, the wave energy spectrum in SWAVE is defined as discrete directional components,

with the spherical convention defining a reference direction at the local east and each component is calculated as a scalar. When a local gradient is calculated, this scalar assumption treats the corresponding vector components at two adjacent cells or nodes as having the same direction (Li, 2012). As waves propagate toward the Pole, the meridian convergence induces an increasing directional difference between the local east directions of two adjacent nodes (Li, 2012; Tolman and the WAVEWATCHIII®Development Group, 2014).

Meridian convergence at the North Pole makes the spherical coordinate equations of SWAVE invalid (Chen et al., 2013). There, longitude does not have a unique value and wave direction cannot be defined, which is a singularity issue at the Pole. When the Global-FVCOM was developed, the singularity issue at the Pole was solved by using the spherical-stereographic conversion coordinate system (Chen et al., 2009; Gao et al., 2011; Chen et al., 2013). However, because of the directional feature of wave energy, the spherical-stereographic conversion coordinate system needs to be modified and deployed to the global wave model.

Two popular approaches are widely used to avoid the North Pole problem in the spherical coordinate system. One is the so-called "grid rotation" by which a new spherical grid is defined on a rotated coordinate system with the North Pole on land (e.g., MOM) (Eby and Holloway, 1994; Pacanowski and Griffies, 2000). This method is simple and costless in terms of needed code modification, but as pointed out by Pacanowski and Griffies (2000), it may make the post-processing of model results complicated, particularly for current vectors. The other is the pole stereographic projection by which all variables in the spherical coordinate system are projected to the well-defined Cartesian polar coordinate system so that the governing equations can be solved while avoiding the singularity issue at the North Pole and the limitation due to the convergence of longitude lines (Phillips, 1957). This method is accurate, but limited to a regional ocean. Multi-projection methods are required to cover northern and southern hemispheres for the global ocean.

Following the spherical-stereographic conversion coordinate system at the North Pole in Global-AO-FVCOM (Gao et al., 2011), we configured SWAVE with symmetric triangular grids within 13 circles originating from the North Pole: 8 triangles in the first circle connecting to the North Pole, and progressively more triangles in succeeding circles, with up to 148 triangles in the thirteenth circle. This is the first time that FVCOM-SWAVE is extended to the North Pole. The original Global-AO-FVCOM scalars (e.g. temperature, salinity, etc.) were first calculated based on a control volume composed of 8 triangles connected to the Pole on stereographic coordinates (Fig. A.1b) and then converted back to the spherical coordinates (Fig. A.1a). In common wave models, the wave spectra were dispersed into scalar bins, and the bins still retain directional properties. If the wave spectra were simply treated as scalars in the spherical coordinate, the directions of the currents would not match the directions of the wave spectra in the control volume with its center at the North Pole. To avoid this issue, the stereographic coordinate system was designed for the 8 triangles connected to the North Pole (Fig. A.1), in which the northward direction of the North Pole points to 180°. The directions of the wave spectrum, ambient current velocity and wave group velocity should be uniformly unified to this stereographic coordinate. The advection of the wave energy spectrum is first simulated in this coordinate system and then converted back to the spherical coordinates. This approach was directly adopted from the spherical-coordinate FVCOM system, and the detailed mathematics can be found in Chen et al. (2013). Taking advantage of the flexibility of the unstructured grid, this method allows SWAVE to run directly on the spherical coordinates for basin, or even global scale ocean applications, without the need for "grid rotation" or "multi-projections".

In addition to the singularity issue, the meridian convergence induces an increasing directional difference between the local east directions of two adjacent nodes. This occurs when the difference in longitude between two adjacent nodes in the control volume is larger than $\frac{180^\circ}{N_D}$ (where N_D is the number of angular bins). In this study, N_D was set to 36 and $\frac{180^\circ}{N_D} = 5°$, and adjacent nodes with latitudes lower than 85°N are not impacted by meridian convergence. Li (2012) introduced a method to solve this problem for wave models. Specifically, the transfer of the local east is mapped to east as defined in the form,

$$\hat{\theta} = \mathrm{sgn}(\cos\varphi \sin\lambda)\cos^{-1}\left[\frac{\cos\lambda\sin\varphi}{\sqrt{1-(\cos\lambda\sin\varphi)^2}}\right], \tag{A.1}$$

In high-latitude regions, the major issue is the mismatch of the local east directions between the coordinate systems of two adjacent nodes. This issue, however, does not happen everywhere on the varying-resolution unstructured grid system. Thus, to reduce the computational demand, a simple criterion was implemented in SWAVE. In SWAVE, the treatment starts with a latitude threshold according to the property of the mesh grid. The treatment is only made when the latitude difference between two adjacent nodes is less that the threshold value, with the modification being made according to the latitude difference between two adjacent nodes. This approach takes advantage of the unstructured grid's ability to improve computational efficiency in global wave simulations. In our method, both the local east directions of the group velocity and the wave spectrum are transferred when the criterion is satisfied. In particular, assuming A and B are two adjacent nodes, before computing the wave energy flux between A and B, we first calculate the longitude difference between the adjacent nodes using

$$\hat{\theta} = \hat{\theta}_B - \hat{\theta}_A. \tag{A.2}$$

If $\hat{\theta} > \frac{180^\circ}{N_D}$, the direction difference between the local east directions of two adjacent nodes should not be ignored. In this case, the treatment should be made. The individual wave direction segment is equal to $\frac{360^\circ}{N_D}$. The corresponding direction segments of A and B are determined by the rotated angles $\hat{\theta}_A$ and $\hat{\theta}_B$ given as

$$K_A = K_B + \Delta K = K_B + \mathrm{ROUND}\left(\frac{\hat{\theta}}{360/N_D}\right), \tag{A.3}$$

where K_A and K_B are the direction segment indexes at A and B, and ΔK is the direction segment difference due to the longitude difference between A and B. ROUND(x) is a function that rounds off the quantity in the brackets to the nearest integer. The advection of wave energy is then calculated based on the corresponding direction segments.

To test the modified SWAVE code, we conducted an idealized case experiment under a constant wind forcing condition. The experiment was made on a flat bottom computational domain with a center at the North Pole in the spherical coordinate system. The domain was configured with an unstructured triangular grid with a minimum horizontal resolution of ~10 km and a boundary at 78°N (Fig. A.2). The mean water depth is 1000 m everywhere. This is a barotropic ocean case with no sea ice. The model was driven by a constant wind of 5 m/s (parallel to 90°E–90°W meridian) at the sea surface (Fig. A.2) and ran for a total of 5 days. To validate the model, we ran this idealized case by turning on and off the correction methodology listed above, and comparisons were made for these two runs.

Fig. A.3 shows snapshots of the distributions of the wave direction at the end of the 24-h simulation with and without the inclusion of the correction treatment. In this case, driven by a uniformly distributed constant wind, the surface waves should propagate in the same direction everywhere. It is clear that without the correction, the surface waves tend to converge in the region where the latitude is higher than 89 degrees, with an unrealistic direction at the North Pole (Fig. A.3: upper panel). The energy convergence in the high latitude region and the energy accumulation at the North Pole become worse with longer integration times. These issues disappear after the correction treatments are turned on (Fig. A.3: lower panel). This result indicates that the treatment method implemented into SWAVE is capable of correcting issues caused by the meridian convergence and North Pole singularity.

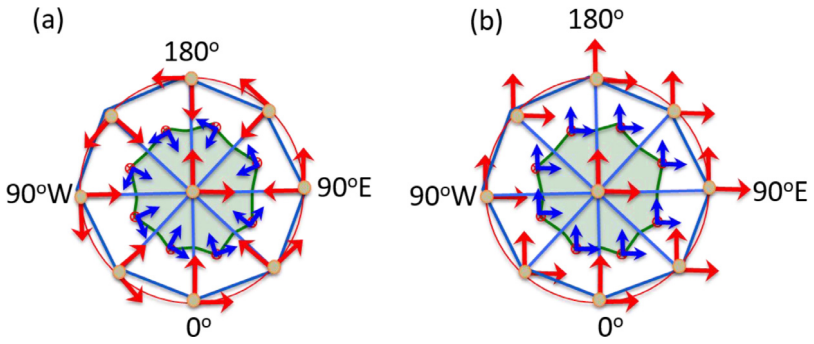

Fig. A.1. Illustrations of the eight triangles specified for the spherical-stereographic conversion coordinate system at the North Pole. (a) The local spherical coordinates and (b) converted stereographic coordinates.

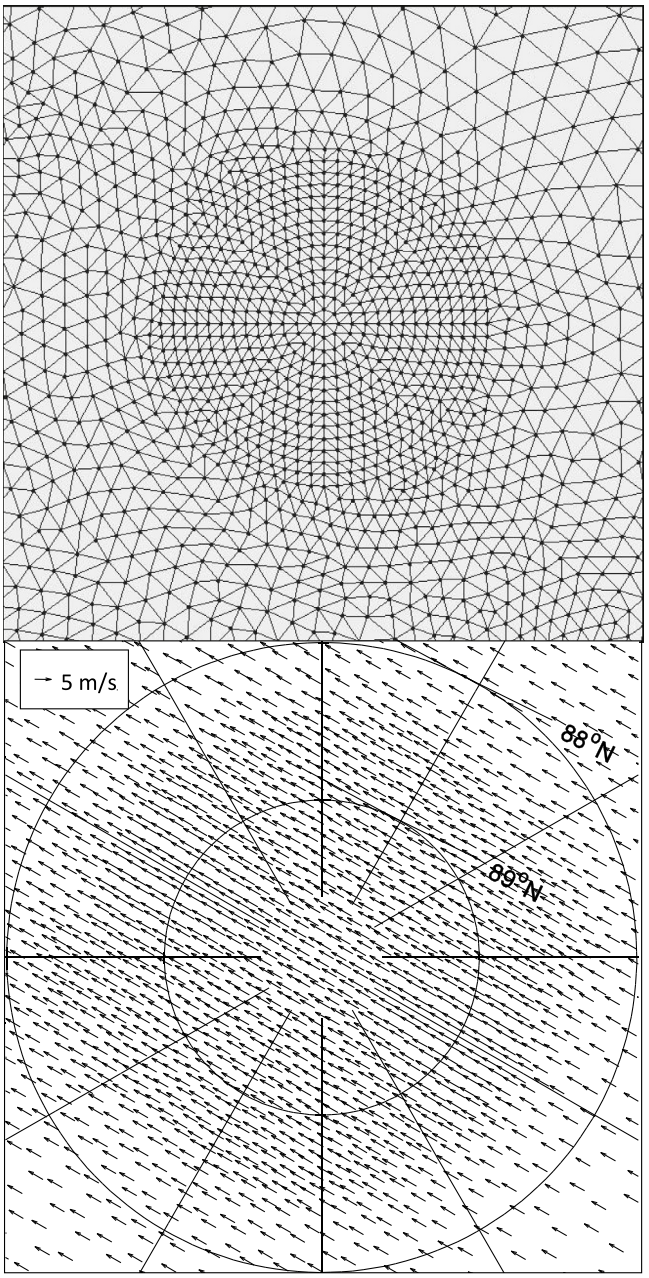

Fig. A.2. Upper panel: Illustration of the unstructured grid around the North Pole region. Lower panel: the distribution of the surface wind velocity vectors (m/s) used in the experiment.

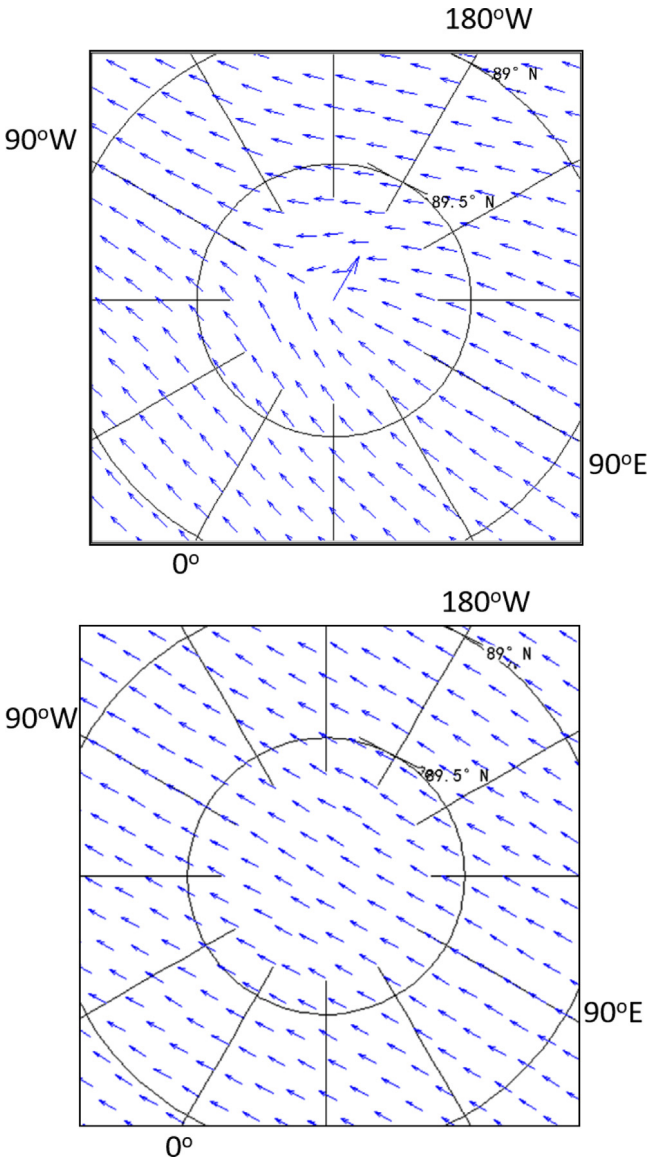

Fig. A.3. A snapshot of the distributions of the wave direction after the first 24-h simulation for the case without (upper panel) and with (lower panel) the treatments of high-latitude invalid scalar assumption and singularity at the North Pole.

Appendix B. Method to track the origin of swell waves in space and time

In the ocean, surface waves disperse and evolve into swell after propagating out of their generation area. In general, swell waves are weakly dissipated and can propagate across an ocean basin over a spatial scale of ~10^4 km (Barber and Ursell, 1948; Snodgrass et al., 1966; Munk et al., 1963). Small amplitude swell waves can be persistent with an energy decay e-folding scale of >2×10^4 km (Ardhuin et al., 2009): half of earth's perimeter. Therefore, swells generated in one region may carry wave energy across the entire ocean (Alves, 2006).

According to wave dispersion theory, swell waves with different frequencies belonging to the same swell group arrive at the same location at different times. The wave group velocity can be determined by either $C_g = \frac{g}{2\omega}$ or $C_g = \frac{d}{\Delta t}$, where d is the distance between locations where waves were observed and generated; g is the gravitational acceleration; ω is the angular frequency of the wave and Δt is the time over which the wave has traveled. The slope shown in Fig. 14 of the swell vector $\frac{df}{dt}$ is related to the travel distance of the swell group ($\frac{df}{dt} = \frac{g}{4\pi d}$), and therefore $d = \frac{g}{4\pi}\frac{dt}{df}$. The original time at which the swell was generated is $t_0 = -f_s\frac{dt}{df}$, where f_s is the peak frequency at the time when this swell group was first observed. Given d, $\bar{\theta}$ (the mean swell direction), λ_s (longitude) and φ_s (latitude) at the observation site, the location (λ_g, φ_g) where the swell group was originally generated can be determined by

$$\lambda_g = \sin^{-1}\left(\sin\lambda_s\cos\omega_d + \sin\omega_d\cos\lambda_s\cos\bar{\theta}\right), \tag{B.1}$$

$$\varphi_g = \varphi_s - \sin^{-1}\left(\frac{\sin\omega_d\sin\bar{\theta}}{\cos\lambda_g}\right), \tag{B.2}$$

$$\omega_d = \frac{d}{R_E}, \tag{B.3}$$

where R_E is the Earth's radius and ω_d is the angular travel distance of the wave.

References

Alves, J.H.G.M., 2006. Numerical modeling of ocean swell contributions to the global wind-wave climate. Ocean Model. 11, 98–122.

Ardhuin, F., Chapron, B., Collard, F., 2009. Observation of swell dissipation across oceans. Geophys. Res. Lett. 36 (6), 150–164.

Ardhuin, F., Sutherland, P., Doble, M., Wadhams, P., 2016. Ocean waves across the Arctic: Attenuation due to dissipation dominates over scattering for periods longer than 19 s. Geophys. Res. Lett. 43 (11), 5775–5783.

Barber, N.F., Ursell, F., 1948. The generation and propagation of ocean waves and swell. I: Wave periods and velocities. Philos. Trans. R. Soc. Lond. 240A, 527–560.

Bidlot, J.R., 2012. Present status of wave forecasting at ECMWF. In: Proceeding from the ECMWF Workshop on Ocean Waves, 25–27, June 2012.

Booij, N., Ris, R.C., Holthuijsen, L.H., 1999. A third-generation wave model for coastal regions: 1. Model description and validation. J. Geophys. Res. 104 (C4), 7649–7666.

Casas-Prat, M., Wang, X.L., Swart, N., 2018. CMIP5-based global wave climate projections including the entire Arctic Ocean. Ocean Model. 123, 66–85, S1463500317301981.

Cavalieri, D.J., Parkinson, C.L., Vinnikov, K.Y., 2003. 30-Year satellite record reveals contrasting Arctic and Antarctic decadal sea ice variability. Geophys. Res. Lett. 30 (18), CRY 4-1.

Chao, Y.Y., Buroughs, L.D., Tolman, H.L., 2004. Wave forecasting for alaskan waters. In: Technical Procedures Bulletin Series No. 496. National Weather Service, NOAA, U.S. Department of Commerce, (Available at http://polar.ncep.noaa.gov/mmab/tpbs/operational.tpbs/tpb496/tpb496.htm).

Chen, C., Beardsley, R.C., Cowles, G., 2006. An unstructured-grid finite-volume coastal ocean model, FVCOM system. Oceanography 19 (1), 78–89.

Chen, C., Beardsley, R.C., Cowles, G., Qi, J., Lai, Z., Gao, G., Stuebe, D., Liu, H., Xu, Q., Xue, P., Ge, J., Ji, R., Hu, S., Tian, R., Huang, H., Wu, L., Lin, H., Sun, Y., Zhao, L., 2013. An Unstructured-Grid, Finite-Volume Community Ocean Model FVCOM User Manual, SMAST/UMASSD Technical Report-13-0701, third ed. University of Massachusetts-Dartmouth, p. 404.

Chen, C., Gao, G., Qi, J., Proshutinsky, A., Beardsley, R.C., Kowalik, Z., Lin, H., Cowles, G., 2009. A new high-resolution unstructured grid finite volume Arctic Ocean model, AO-FVCOM): An application for tidal studies. J. Geophys. Res.: Oceans 114 (C8).

Chen, C., Gao, G., Zhang, Y., Beardsley, R.C., Lai, Z., Qi, J., H. Lin, H., 2016. Circulation in the Arctic Ocean: results from a high-resolution coupled ice-sea nested Global-FVOM and Arctic-FVCOM system. Prog. Oceanogr. 141, 60–80. http://dx.doi.org/10.1016/j.pocean.2015.12.002.

Chen, C., Liu, H., Beardsley, R.C., 2003. An unstructured grid, finite-volume, three-dimensional, primitive equations ocean model: application to coastal ocean and estuaries. J. Atmos. Oceanic Tech. 20 (1), 159.

Collins, C.O., Rogers, W.E., Marchenko, A., Babanin, A.V., 2015. In situ measurements of an energetic wave event in the Arctic marginal ice zone. Geophys. Res. Lett. 42 (6), 1863–1870.

Comiso, J.C., 2006. Abrupt decline in the Arctic winter sea ice cover. Geophys. Res. Lett. 33 (18), 488–506, L1850418.

Comiso, J.C., Parkinson, C.L., Gersten, R., Stock, L., 2008. Accelerated decline in the Arctic sea ice cover. Geophys. Res. Lett. 35 (1), 179–210.

Dean, C.H., 1966. The attenuation of ocean waves near the open ocean/pack ice boundary. In: Symposium on Antarctic Oceanography. Scientific Committee on Antarctic Research, Santiago, Chile, pp. 13–16, Sept..

Doble, M.J., Bidlot, J., 2013. Wave buoy measurements at the Antarctic sea ice edge compared with an enhanced ECMWF WAM: Progress towards global waves-in-ice modelling. Ocean Model. (ISSN: 1463-5003) 70, 166–173. http://dx.doi.org/10.1016/j.ocemod.2013.05.012.

Dumont, D., Kohout, A., Bertino, L., 2011a. A wave-based model for the marginal ice zone including a floe breaking parameterization. J. Geophys. Res. 116 (C4), 241–253.

Dumont, D., Kohout, A., Bertino, L., Sandven, S., 2011b. A model for waves-in-ice and sea ice dynamics in the marginal ice zone. In: Arctic Tech. Conference, OTC-22049.

Eby, M., Holloway, G., 1994. Grid transformation for incorporating the Arctic in a global ocean model. Clim. Dynam. 10 (No. 4–5), http://dx.doi.org/10.1007/BF00208991.

ECMWF, 2014. IFS DOCUMENTATION - Cy40R1, Operational implementation 22 November 2013, PART VII: Wave Model, ECMWF IFS documentation.

Gao, G., Chen, C., Qi, J., Beardsley, R.C., 2011. An unstructured-grid, finite-volume sea ice model: development, validation, and application. J. Geophys. Res.: Oceans 116 (C8), 295–308.

Haas, C., Lobach, J., Hendricks, S., Rabenstein, L., Pfaffling, A., 2009. Helicopter-borne measurements of sea ice thickness, using a small and lightweight, digital EM system. J. Appl. Geophys. 67 (3), 234–241.

Hanson, J.L., Phillips, O.M., 2001. Automated analysis of ocean surface directional wave spectra. J. Atmos. Oceanic Technol. 18, 277–293.

Hanson, J.L., Tracy, B.A., Tolman, H.L., Scott, R.D., 2009. Pacific hindcast performance of three numerical wave models. J. Atmos. Oceanic Tech. 26 (8), 1614–1633.

Hasselmann, K., 1962. On the non-linear energy transfer in a gravity-wave spectrum part 1. general theory. J. Fluid Mech. 12, 481–500.

Hasselmann, K., Barnett, T.P., Bouws, E., Carlson, H., Cartwright, D.E., Enke, K., et al., 1973. Measurements of wind-wave growth and swell decay during the joint north sea wave project, JONSWAP. Dtsch. Hydrogr. Z. A9 (12), 95.

Hunke, E.C., Lipscomb, W.H., 2006. CICE: The Los Alamos Sea Ice Model Documentation and Software User'S Manual. Report, Los Alamos Natl. Lab., Los Alamos, N. M..

Keller, J.B., Weitz, M., 1953. Reflection and transmission coefficients for waves entering or leaving an icefield. Comm. Pure Appl. Math. 6 (3), 415–417.

Kohout, A.L., Meylan, M.H., 2008. An elastic plate model for wave attenuation and ice floe breaking in the marginal ice zone. J. Geophys. Res. 113, C09016. http://dx.doi.org/10.1029/2007JC004434.

Kohout, A.L., Williams, M.J.M., Dean, S.M., Meylan, M.H., 2014. Storm-induced sea-ice breakup and the implications for ice extent. Nature 509 (7502), 604–607.

Krinner, G., Rinke, A., Dethloff, K., Gorodetskaya, I.V., 2010. Impact of prescribed Arctic sea ice thickness in simulations of the present and future climate. Clim. Dyn. 35, 619–633.

Kwok, R., Cunningham, G., Wensnahan, M., Rigor, I., Zwally, H., Yi, D., 2009. Thinning and volume loss of the Arctic Ocean sea ice cover: 2003–2008. J. Geophys. Res.: Oceans 114, C07005. http://dx.doi.org/10.1029/2009JC005312.

Li, J., 2012. Propagation of ocean surface waves on a spherical multiple-cell grid. J. Comput. Phys. (ISSN: 0021-9991) 231 (24), 8262–8277. http://dx.doi.org/10.1016/j.jcp.2012.08.007.

Li, J., Kohout, A.L., Shen, H.H., 2015. Comparison of wave propagation through ice covers in calm and storm conditions. Geophys. Res. Lett. 42, 5935–5941.

Li, J., Saulter, A., 2014. Unified global and regional wave model on a multi-resolution grid. Ocean Dynam. 64 (11), 1657–1670.

Liu, A.K., Mollo-Christensen, E., 1988. Wave propagation in a solid ice pack. J. Phys. Oceanogr. 18 (11), 1702–1712.

Liu, A.K., Peng, C.Y., Vachon, P.W., 1991. Wave attenuation in the marginal ice zone during LIMEX. Atmos. Ocean 30 (2), 192–206.

Masson, D., LeBlond, P., 1989. Spectral evolution of wind-generated surface gravity waves in a dispersed ice field. J. Fluid. Mech. 202, 43–81.

Meier, W., Stroeve, J., Fetterer, F., Knowles, K., 2005. Reductions in Arctic sea ice cover no longer limited to summer. EOS Trans. Am. Geophys. Union 86 (36), 326.

Meylan, M.H., Masson, D., 2006. A linear Boltzmann equation to model wave scattering in the marginal ice zone. Ocean Model. 11, 417–427.

Munk, W.H., Miller, G.R., Snodgrass, F.E., Barber, N.F., 1963. Directional recording of swell from distant storms. Philos. Trans. R. Soc. Lond. Ser. A 255, 505–584.

Pacanowski, R., Griffies, S.M., 2000. MOM 3.0 manual. p. 353, http://www.gfdl.noaa.gov/~smg/mom/web/guide_parent//guide_parent.html.

Perrie, W., Hu, Y., 1996. Air-ice-ocean momentum exchange. Part I: Energy transfer between waves and ice floes. J. Phys. Oceanogr. 26 (9), 1705–1720.

Peters, A.S., 1950. The effect of a floating mat on water waves. Comm. Pure Appl. Math. 3 (4), 319–354.

Phillips, N., 1957. A map projection system suitable for large-scale numerical weather prediction. J. Meteor. Soc. Japan. 75, 262–267.

Qi, J., Chen, C., Beardsley, R.C., Perrie, W., Cowles, G.W., Lai, Z., 2009. An unstructured-grid finite-volume surface wave model, (FVCOM-SWAVE): Implementation, validations and applications. Ocean Model. (ISSN: 1463-5003) 28 (1–3), 153–166. http://dx.doi.org/10.1016/j.ocemod.2009.01.007.

Robin, G. de Q., 1963. Wave propagation through fields of pack ice. Philos. Trans. R. Soc. Lond. Ser. A 255 (1057), 313–339.

Romanov, I.P., 1995. Atlas of Ice and Snow of the Arctic Basin and Siberian Shelf Seas, second ed. Backbone, Paramus, N. J., translated from Russian by A. Tunik.

Shapiro, A., Simpson, L.S., 1953. The effect of a broken icefield on water waves. Trans. Am. Geophys. Union. 34 (1), 36–42.

Smith, M., Thomson, J., 2016. Scaling observations of surface waves in the Beaufort Sea. 4:000097.

Snodgrass, F.E., Groves, G.W., Hasselmann, K., Miller, G.R., Munk, W.H., Powers, W.H., 1966. Propagation of ocean swell across the pacific. Philos. Trans. R. Soc. Lond. Ser. A 249, 431–497.

Squire, V.A., 2007. Of ocean waves and sea–ice revisited. Cold Reg. Sci. Technol. 49, 110–133.

Squire, V.A., Dugan, J.P., Wadhams, P., Rottier, P.J., Liu, A.K., 1995. Of ocean waves and sea ice. Annu. Rev. Fluid Mech. 27, 115–168.

Squire, V.A., Moore, S.C., 1980. Direct measurement of the attenuation of ocean waves by pack ice. Nature 5745, 365–368.

Squire, V.A., Vaughan, G.L., Bennetts, L.G., 2009. Ocean surface wave evolvement in the Arctic Basin. Geophys, Res. Lett. 36 (22), 355.

Stephenson, S.R., Smith, L.C., Agnew, J.A., 2011. Divergent long-term trajectories of human access to the Arctic. Nat. Clim. Chang. 1 (3), 156–160.

SWAN Team, 2006a. SWAN Cycle III Version 40.51 Technical Documentation. Delft University of Technology, Faculty of Civil Engineering and Geosciences, Environmental Fluid Mechanics Section, P.O. Box 5048, 2600 GA Delft, The Netherlands.

SWAN Team, 2006b. SWAN Cycle III Version 40.51 User Manual. Delft University of Technology, Faculty of Civil Engineering and Geosciences, Environmental Fluid Mechanics Section, P.O. Box 5048, 2600 GA Delft, The Netherlands.

Thomson, J., Rogers, W.E., 2014. Swell and sea in the emerging Arctic Ocean. Geophys. Res. Lett. 41, 3136–3140. http://dx.doi.org/10.1002/2014GL059983.

Thomson, J., et al., 2016. Emerging trends in the sea state of the Beaufort and Chukchi seas. Ocean Model. 105, 1–12. http://dx.doi.org/10.1016/j.ocemod.2016.02.009.

Tolman, H.L., 2003. Treatment of unresolved islands and ice in wind wave models. Ocean Model. 4, 219–231.

Tolman, H.L., 2009. User Manual and System Documentation of WAVEWATCH III TM Version 3.14. Tech. Note 276, NOAA/NWS/NCEP/MMAB, p. 194.

Tolman, H.L., Balasubramaniyan, B., Burroughs, L.D., Chalikov, D.V., Chao, Y.Y., Chen, H.S., Gerald, V.M., 2002. Development and implementation of wind generated ocean surface wave models at NCEP. Weather Forecast. 17, 311–333.

Tolman, H.L., the WAVEWATCHIII®Development Group, 2014. User Manual and System Documentation of WAVEWATCHIII®Version 4.18. NCEP Technical Rep. MMAB Contribution No. 316, p. 311, Available at https://polar.ncep.noaa.gov/waves/wavewatch/manual.v4.18.pdf.

Wadhams, P., Squire, V.A., Ewing, J.A., Pascal, R.W., 1986. The effect of the marginal ice zone on the directional wave spectrum of the ocean. J. Phys. Oceanogr. 16 (2), 358–376.

Wadhams, P., Squire, V.A., Goodman, D.J., Cowan, A.M., Moore, S.C., 1988. The attenuation of ocean waves in the marginal ice zone. J. Geophys. Res. 93 (C6), 6799–6818.

Wang, X.L., Feng, Y., Swail, V.R., Cox, A., 2015. Historical changes in the Beaufort-Chukchi-Bering seas surface winds and waves, 1971–2013. J. Clim. 28, 7457–7469.

Weber, J.E., 1987. Wave attenuation and wave drift in the marginal ice zone. J. Phys. Oceanogr. 17 (12), 2351–2361.

Wentz, F.J., 2013. SSM/I Version-7 Calibration Report. Report Number 011012, Remote Sensing Systems, Santa Rosa, CA, p. 46.

Williams, T.D., Bennetts, L.B., Squire, V.A., Dumont, D., Bertino, L., 2013a. Wave-ice interactions in the marginal ice zone Part 1: Theoretical foundations. Ocean Model. (ISSN: 1463-5003) 71, 81–91. http://dx.doi.org/10.1016/j.ocemod.2013.05.010.

Williams, T.D., Bennetts, L.B., Squire, V.A., Dumont, D., Bertino, L., 2013b. Wave-ice interactions in the marginal ice zone Part 2: Numerical implementation and sensitivity studies along 1D transects of ocean surface. Ocean Model. (ISSN: 1463-5003) 71, 92–101. http://dx.doi.org/10.1016/j.ocemod.2013.05.011.

Zhang, Y., Chen, C., Beardsley, R.C., Gao, G., Lai, Z., Curry, B., Lee, G.M., Lin, H., Qi, J., Xu, Q., 2016a. Studies of the Canadian Arctic Archipelago water transport and its relationship to basin-local forcing: results from AO-FVCOM. J. Geophys. Res.-Ocean 121, http://dx.doi.org/10.1002/2016JC011634.

Zhang, Y., Chen, C., Beardsley, R.C., Gao, G., Qi, J., Lin, H., 2016b. Seasonal and interannual variability of the Arctic sea ice: a comparison between AO-FVCOM and observations. J. Geophys. Res.-Ocean 121 (11).